Helmholtz-Zentrum
Geesthacht
Zentrum für Material- und Küstenforschung

Original

Stanev, E.V.; Ziemer, F.; Schulz-Stellenfleth, J.; Seemann, J.; Staneva, J.; Gurgel, K.:
Blending Surface Currents from HF Radar Observations and Numerical Modeling: Tidal Hindcasts and Forecasts.
In: Journal of Atmospheric and Oceanic Technology. Vol. 32 (2015) 2, 256 - 281.
First published online by AMS: 01.02.2015

https://dx.doi.org/10.1175/JTECH-D-13-00164.1

Blending Surface Currents from HF Radar Observations and Numerical Modeling: Tidal Hindcasts and Forecasts

E. V. STANEV, F. ZIEMER, J. SCHULZ-STELLENFLETH, J. SEEMANN, AND J. STANEVA

Institute of Coastal Research, Helmholtz-Zentrum Geesthacht, Geesthacht, Germany

K.-W. GURGEL

Institute of Oceanography, University of Hamburg, Germany

(Manuscript received 12 August 2013, in final form 15 October 2014)

ABSTRACT

An observation network operating three Wellen Radars (WERAs) in the German Bight, which are part of the Coastal Observing System for Northern and Arctic Seas (COSYNA), is presented in detail. Major consideration is given to expanding the patchy observations over the entire German Bight on a 1-km grid and producing state estimates at intratidal scales, and 6- and 12-h forecasts. This was achieved with the help of the proposed spatiotemporal optimal interpolation (STOI) method, which efficiently uses observations and simulations from a free model run within an analysis window of one or two tidal cycles. In this way the method maximizes the use of available observations and can be considered as a step toward the ''best surface current estimate.'' The performance of the analysis was investigated based on the achieved reduction of the misfit between model and observations. The complex dynamics of the study domain was illustrated based on the spatial and temporal changes of tidal ellipses for the M_2 and M_4 constituents from HF radar observations. It was demonstrated that blending observations and numerical modeling facilitates physical interpretation of processes such as the nonlinear distortion of the Kelvin wave in the coastal zone and in particular in front of the Elbe and Weser estuaries. Comparisons with in situ data acquired outside the area covered by the HF radar demonstrated that the analysis method is able to propagate the HF radar information to larger spatial scales.

1. Introduction

The geographical area of the present research is the German Bight in the southern North Sea (Fig. 1), which is characterized by very shallow water, complex bathymetry, and mesotidal conditions. The Coastal Observing System for Northern and Arctic Seas (COSYNA), which was recently deployed in this area, integrates near-real-time measurements with numerical models in a preoperational way and provides continuously coastal ocean state estimates and forecasts. The measurement suite used in the present study includes in situ time series from stationary stations [acoustic Doppler current profiler (ADCP)] and high-frequency (HF) radars. The forecasting suite includes nested 3D hydrodynamic models running in a data assimilation mode that are forced with meteorological forecast data. The aim of this paper is to review the present status of the nowcasting–forecasting system for the German Bight, focusing on the HF radar data assimilation, operational aspects, and product validation.

Hundreds of HF radar systems have been installed worldwide in both operational and experimental modes (Barrick 2008; Harlan et al. 2010; Willis 2012). With their large area coverage, high resolution in time and space, and long-term operational capabilities, they enhanced the coastal ocean monitoring capabilities for surface currents (Paduan and Rosenfeld 1996) and enabled developing new data products. The value of HF radar data for the investigation of circulation in the German Bight was addressed by Carbajal and Pohlmann (2004) and Port et al. (2011). The promising results of these studies have motivated initial steps toward the assimilation of HF radar data into numerical models with the aim of improving ocean hindcasts, nowcasts, and forecasts.

The present study addresses observations, numerical modeling, and a method proposed to carry out the blending of models and HF radar observations in an

Corresponding author address: Emil V. Stanev, Institute of Coastal Research, Helmholtz-Zentrum Geesthacht, Max-Planck-Strasse 1, 21502 Geesthacht, Germany.
E-mail: emil.stanev@hzg.de

DOI: 10.1175/JTECH-D-13-00164.1

© 2015 American Meteorological Society

Brought to you by HELMHOLTZ-ZENTRUM GEESTHACHT | Unauthenticated | Downloaded 03/09/21 08:07 AM UTC

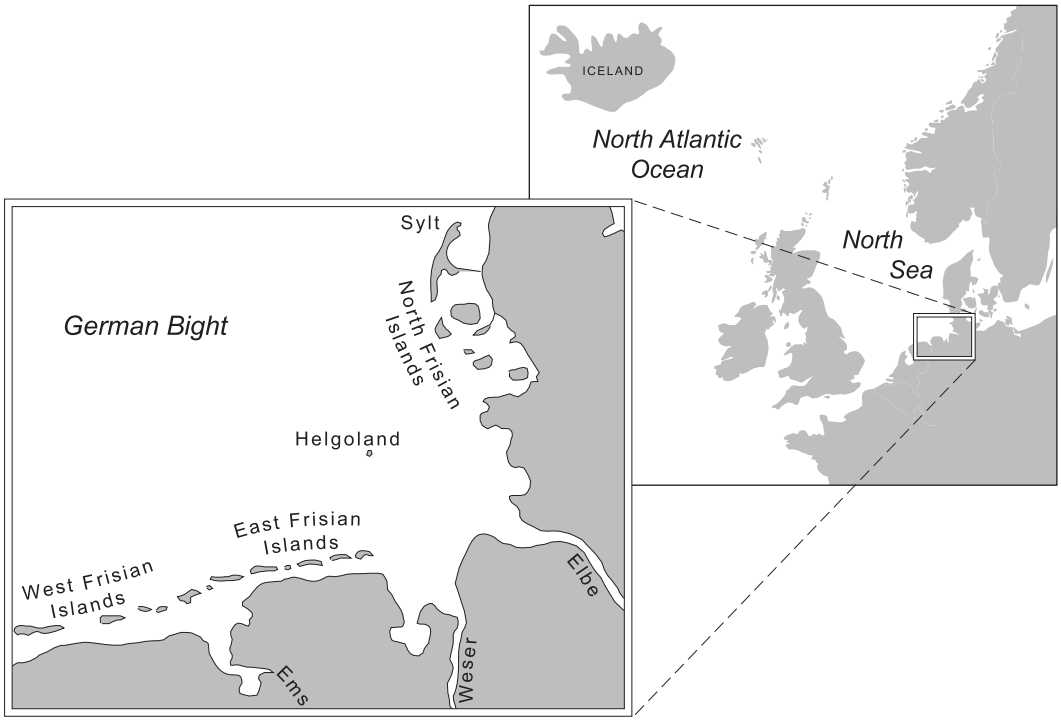

FIG. 1. North Sea and German Bight.

efficient and dynamically consistent way. Assimilation of HF radar data is not a trivial task because of irregular data gaps in time and space, inhomogeneous observation errors, and inconsistency between boundary forcing and observations (Breivik and Saetra 2001; Ivanov and Melnichenko 2005). The techniques used to assimilate HF radar data include optimal interpolation (Gandin 1965; Breivik and Saetra 2001), more sophisticated statistical approaches (Oke et al. 2002; Paduan and Shulman 2004; Barth et al. 2008, 2010; Sakov et al. 2010; Hunt et al. 2004; van Leeuwen 2001), variational methods (Sentchev et al. 2006; Yaremchuk and Sentchev 2009; Scott et al. 2000; Kurapov et al. 2003; Zhang et al. 2010a,b; Li et al. 2008; Moore et al. 2011), and ad hoc approaches (Lewis et al. 1998; Stanev et al. 2011). Introductions to the basic methodologies of the ensemble Kalman filter and three-dimensional variational data assimilation (3DVAR)/4DVAR methods can be found in Evensen (2007) and Bennet (2002). An altogether different methodology to use HF radar data for the computation of forecasts, for example, is presented in Frolov et al. (2012) and Wahle and Stanev (2011), where only observations without numerical model output are taken as input for the analysis.

A major challenge of HF radar assimilation is the treatment of tides. This issue is obviously of particular concern in areas like the German Bight, which are dominated by tidal currents. One approach proposed in literature is to filter out the tidal signal and to use only the residual currents in the analysis (Oke et al. 2002; Kurapov et al. 2003; Wilkin et al. 2005). This approach was not followed in this study, because it turned out that the model errors on intratidal time scales can be successfully corrected by the HF radar, that is, filtering of the data would mean a waste of a lot of information. Approaches to assimilate HF radar data on tidal and intratidal time scales have been proposed, for example, using optimal interpolation (Breivik and Saetra 2001) or nudging techniques (Gopalakrishnan and Blumberg 2012).

Classical assimilation filter approaches like optimal interpolation or 3DVAR perform an analysis and a model restart each time new observations become available. For HF radar data, which are typically acquired several times per hour, this means that it is difficult for the model to reach equilibrium between two analysis time steps. Furthermore, assimilation filters produce discontinuous state trajectories, which are particularly undesirable for the highly dynamic current fields in tide-dominated areas.

The method presented here uses a spatiotemporal optimal interpolation filter to improve short-term hindcasts and forecasts of surface currents. The approach uses elements of both classical assimilation filters and techniques, which use observations alone (e.g., Frolov et al.

Brought to you by HELMHOLTZ-ZENTRUM GEESTHACHT | Unauthenticated | Downloaded 03/09/21 08:07 AM UTC

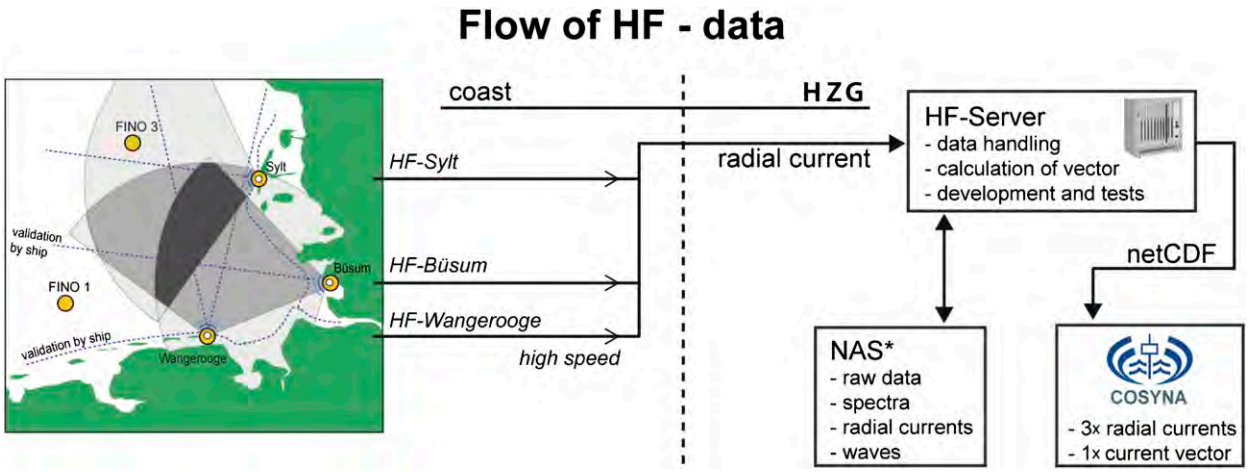

FIG. 2. HF WERA system covering the German Bight. (left) Positions of the three COSYNA HF radar stations: Wangerooge, Büsum, and Sylt. (right) Processing and data flow scheme. Radial current components are transferred to the HZG WERA server. Here, the current vector field is calculated from the radial components and presented on the COSYNA data portal. The radar data are stored on a NAS system.

2012; Wahle and Stanev 2011). In the proposed approach, model simulations from a free run and radar observations acquired over periods of at least one tidal cycle were blended using the Kalman analysis equation. The focus on intratidal time scales and the data assimilation technique used here explain the major differences from some earlier studies using 1) filtered data and 2) the classical Kalman analysis method, where observations and numerical simulations are usually combined at individual time steps. The proposed data assimilation approach has similarities with the methods described in Barth et al. (2010) and Sakov et al. (2010). However, it uses a simpler formulation of the model error covariance matrix, but at the same time addresses the forecast capability.

The focus on intratidal scales can be justified by the need to 1) develop a better knowledge on the short-term coastal ocean variability and 2) enhance the quality of data needed for specific operations. One example is the performance of oil spill predictions, which depends on how good the circulation during and after the spill event is known. It is also important to know how prediction errors depend on the inaccuracy of the known state. Similar is the situation with search and rescue operations (Frost and Stone 2001; Hackett et al. 2006), which also needs high-quality short-term predictions. Thus, the evaluations provided here are aimed at demonstrating the improvement of predictions as a result of the improved ocean state due to assimilation of HF radar data.

In section 2 we present the HF radar array, its infrastructure, and results from observations. The nested numerical model system is presented in section 3 and data assimilation in section 4. Section 5 addresses the analysis of hindcasts, followed by results and discussion in section 6 and conclusions in section 7.

2. The coastal observatory: Focus on the HF radar observations

a. *Overall description of the observations*

COSYNA, which is operated by the Institute of Coastal Research, Helmholtz-Zentrum Geesthacht (HZG) in cooperation with the German Marine Research Consortium, shows many similarities with other advanced coastal observatories in the United States and Europe (e.g., Glenn and Schofield 2009; Proctor and Howarth 2008). It consists of observational nodes, a data management system, and data assimilation capabilities, streamlined toward meeting the needs for high-quality operational products in the German Bight. The individual in situ observing subsystems used here are fixed sensor platforms. At some locations [e.g., Forschungsplattformen in Nord- und Ostsee 1 and 3 (FINO-1 and FINO-3, respectively)] ADCPs are installed (see Fig. 2). Remote sensing includes HF radar stations. Satellite altimeter data, a commonly used information source in global and regional ocean data assimilation, are not used in the present research because we address here short-term tidal state estimates and predictions; however, the repeat cycles of the *Environmental Satellite* (*Envisat*) and *Jason-2* are 35 and 9.9156 days, respectively. The second reason not to use altimeter data is that their amount over the German Bight is very small in comparison to the amount of HF radar observations (see further in text). The third reason is that the quality of altimeter observations in the coastal ocean is not very good. However, we admit that ascending/descending passes provide some

Brought to you by HELMHOLTZ-ZENTRUM GEESTHACHT | Unauthenticated | Downloaded 03/09/21 08:07 AM UTC

useful information (Schulz-Stellenfleth and Stanev 2010) that could motivate further research on incorporating altimeter data into coastal operational forecasting.

Data management and provision (Fig. 2), including implementation of quality control focused on near-real-time enhancements, storage, and delivery, as well as data archiving, ensure the capability for HF radar data to be integrated into operational practice. COSYNA follows an open data policy. Data format convergence is achieved through metadata mapping. The metadata are based on the German Nord- und Ostsee Küsteninformationssystem (NOKIS, which stands for coastal information system for the North and Baltic Seas) standard. Data products include real-time or near-real-time data generated from in situ observing or remote sensing systems, and nowcasts and forecasts described further in the paper.

b. *HF radar system*

1) HF RADAR NETWORK

An ocean surface current transporting the Bragg resonant ocean waves causes a Doppler shift (Barrick 1978; Stewart and Joy 1974). This shift can be converted to the underlying current speed toward or away from the radar, which is the radial component u_r of the two-dimensional (2D) surface current. Based on this principle, three HF radars have been installed on the island of Wangerooge, at Büsum (in some of the figures also referred to as ''Buesum''), and on the island of Sylt (Fig. 2) to monitor ocean currents and waves in the German Bight. These systems cover the eastern part of the German Bight and are Wellen Radar (WERA)-type radars (Gurgel et al. 1999a,b) operated in the 10.8-MHz (Büsum and Sylt) and 12.1-MHz (Wangerooge) frequency range. Spatial resolution is 1.5 km in range and 3° in azimuth. Because of the working frequency, the radar couples to 12.5-m-long (12.1 MHz) and 13.9-m-long (10.8 MHz) ocean waves by Bragg scattering and the radar echoes provide information on ocean currents within a surface layer of about 1 m (Stewart and Joy 1974; Teague et al. 2001). The working range of the WERAs mainly depends on salinity, sea state, working frequency, and electromagnetic noise [radio frequency interference (RFI), background noise, and ionospheric reflections]. For a table of typical working ranges, see Gurgel and Schlick (2008). The COSYNA WERAs use electromagnetic ground wave propagation and reach out to 120 km off the coast.

2) OCEAN CURRENT RADIAL COMPONENTS

This processing step is done online at each HF radar site of the COSYNA network and provides the radial component of the ocean surface current and its accuracy for a given location on a predefined grid. Locations that are not covered because of a reduced working range caused by limitations in the electromagnetic or oceanographic environmental conditions are left empty.

Within COSYNA, the WERA HF radar is run continuously for 58 min. During this time, the stream of radar echoes from all receive antennas of the linear array is sampled at 0.26-s intervals and stored every 128 samples. This leads to about 33-s lasting coherent fractions, which can later be combined to form longer time series as required for further processing.

Typical integration times for tsunami detection, ocean currents, and ocean wave processing are 2, 9, and 18 min, leading to 512, 2048, and 4096 samples, respectively. The remaining 2 min within an hour are used to scan the frequency range the HF radar is licensed to be operated at and to select the cleanest frequency range with the lowest RFI possible for the next 58-min radar run.

For ocean current processing, time series of 2048 samples are combined and processed in 20-min steps. These time series are then split up into 13 sliding fractions of 512 samples with 75% overlap. The spectra of these fractions are calculated after dynamic recalibration of the antenna gains by normalizing the first-order Bragg power received by each antenna and applying a Blackman–Harris window. By combining the complex spectra from all antennas of the linear array, beam forming is done in the frequency domain. Exactly the same processing is done with the RFI-only signals acquired by the radar. The resulting beam-formed RFI power spectra from the fractional RFI time series are used to mitigate the influence of the RFI on the ocean backscatter spectra for each spectrum before averaging. For more details on the RFI processing, see Gurgel and Schlick (2009).

After RFI mitigation, the beam-formed power spectra from all fractional time series are averaged. This is done for all locations on a radial grid covering the angles from −60° to +60° in 1° steps and on range rings spaced at the radar's range resolution, which is 1.5 km in the case of COSYNA. To transform these average power spectra to a Cartesian grid, a linear interpolation of the spectra from the four range/azimuth locations of the radial grid closest to the Cartesian grid points is done. The processing described above results in cleaned backscatter Doppler spectra for all locations covered by the radar.

In the next step, the peaks in the spectra caused by the first-order Bragg resonance are determined. Problems may arise from spurious peaks caused by ship echoes or remaining RFI. In the following we denote the radial current corresponding to a spectral line i as $u_r(i)$. If two Bragg peaks can be found at $2f_{\mathrm{Bragg}}$ frequency offset between them, then this helps the algorithm to identify the correct peaks. In contrast to direction-finding

Brought to you by HELMHOLTZ-ZENTRUM GEESTHACHT | Unauthenticated | Downloaded 03/09/21 08:07 AM UTC

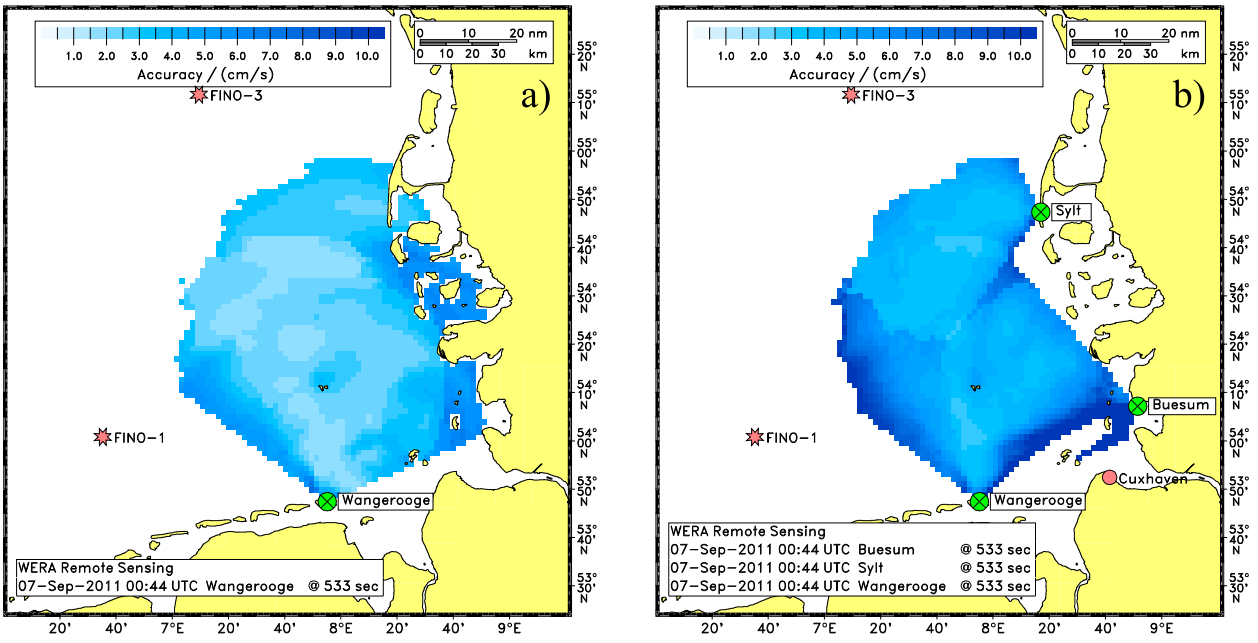

FIG. 3. Accuracy of the radial component of the surface current measured by the HF radar site Wangerooge, as calculated from (a) the ocean echoes by the algorithm described in section 2b(2) and (b) the accuracy of the resulting 2D current, when all three radial components are combined by the weighted least squares algorithm described in section 2b(3).

systems, where all radial current estimates on the radial grid within a search radius around a selected location on the Cartesian grid are used to calculate average and accuracy (cf. section 2.1.1 of Barth et al. 2010), the interpolation from the radial grid to the Cartesian grid is done here by interpolating the Doppler spectra.

The statistics of the current velocity is derived from the width of the first-order Bragg peak(s). The spectral-averaged radial current velocity $\overline{u}_r$ and its accuracy Acc_r are calculated from the Doppler shift of the spectral lines within an interval of $i = \pm 8$ lines around the one or two Bragg peak locations $i_B(j), j = 1, 2$ and their signal-to-noise ratio $S/N(i)$. This interval has been chosen because it represents the first-order Bragg peak; second-order echoes are found farther off the Bragg peak and thus are excluded from the statistics. Within the interval, $K = 17$ contributions for one Bragg peak and $K = 34$ contributions for two Bragg peaks are processed. The algorithm in Barth et al. (2010) has been modified as follows:

$$\overline{u}_r = \frac{\sum_{i=i_B(j)-8}^{i_B(j)+8} u_r(i) S/N(i)}{\sum_{i=i_B(j)-8}^{i_B(j)+8} S/N(i)}. \tag{1}$$

The variance σ_r^2 of $\overline{u}_r$ is calculated as

$$\sigma_r^2 = \frac{\sum_{i=i_B(j)-8}^{i_B(j)+8} u_r(i)^2 S/N(i)}{\sum_{i=i_B(j)-8}^{i_B(j)+8} S/N(i)} - \overline{u}_r^2. \tag{2}$$

Finally, the Acc_r of the $\overline{u}_r$ is calculated as

$$\mathrm{Acc}_r = \frac{\sigma_r}{\sqrt{K}}. \tag{3}$$

Because the value of K is not very large, a correction based on the Student's t distribution is applied. The accuracy of the radial component acquired by the Wangerooge station, as calculated in the way discussed above, is shown in Fig. 3a.

3) 2D CURRENTS FROM RADIAL COMPONENTS

The two and three radial components of the 2D surface current are combined by applying the algorithm initially described by Gurgel (1994) and updated in appendix B of Barth et al. (2010). Along with the radial components $\overline{u}_r$, their standard deviation σ_r is passed to Eq. (B4) in Barth et al. (2010). Solving Eq. (B5) in Barth et al. (2010) gives the meridional and zonal components of the 2D surface current vector. In a next step, the covariance matrix is calculated as shown in Eq. (B6) in Barth et al. (2010). The variance of the meridional and

Brought to you by HELMHOLTZ-ZENTRUM GEESTHACHT | Unauthenticated | Downloaded 03/09/21 08:07 AM UTC

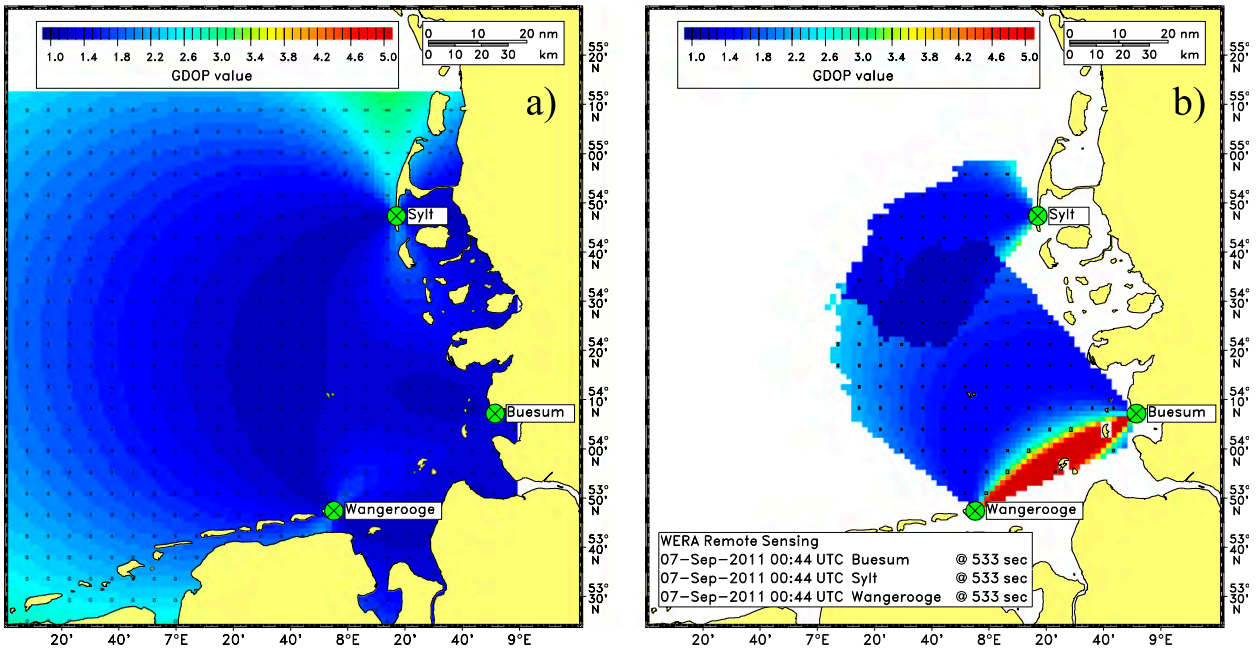

FIG. 4. GDOP (a) for the case in which every location is covered by radial components from all three sites and (b) for the actual measurement. Small rectangles show the meridional and zonal components of the GDOP; absolute value is encoded in color.

zonal components of the 2D surface current $\sigma^2(v)$ and $\sigma^2(u)$ are then found on the diagonal elements of the covariance matrix; $\sigma(v)$ and $\sigma(u)$ finally give the accuracy. An example of the absolute value of the accuracy is shown in Fig. 3b.

The accuracy as calculated above includes the influence of the geometry between the radar sites, which generally is referred to as geometrical dilution of precision (GDOP), and is well known from the satellite navigation system GPS. It is a factor describing the dilution (degrading) of the accuracy of the radial components due to the angles between them. In the case of more than two radial components and advantageous angles between them, the GDOP can be lower than one, thus giving an increased accuracy.

When in the algorithm described above the radial components $\overline{u}_r$ are set to zero with an Acc_r of one, the meridional and zonal components of the GDOP are given by the square root of the diagonal elements of the covariance matrix. In the case where all locations of the predefined Cartesian grid are covered by radial components from all radar sites, large areas show low GDOP values (Fig. 4a). However, normally the working range and azimuthal coverage of the radars is limited and large areas are only covered by two radars. An example of the GDOP resulting from the coverage given by an actual measurement is shown in Fig. 4b. Note that especially the GDOP around the line connecting Wangerooge and Büsum exceeds a value of 5.0, while the GDOP around the line connecting Wangerooge and Sylt is low due to the coverage available from the Büsum radar.

c. *Data management and illustration of system performance*

Radial components of the 2D current are calculated at the radar sites every 20 min. Once available, these are transferred to a central server at HZG by data links, where they are archived and combined to form the 2D current field. The maximum delay from starting the acquisition of the radar echoes to the final current map is 35 min. COSYNA provides a web-based interface to make the radial components and the 2D currents maps available to the public in ASCII and netCDF format. All data are stored on a network-attached storage (NAS) system for further postprocessing and research. Figure 2 illustrates this setup.

Figures 5a–c illustrate the radial surface current measurements acquired at 1823 UTC 10 February 2011 by the three stations along with the derived 2D current vectors (Fig. 5d). For better visualization, current vectors are shown on a coarser grid with 10-km spacing.

d. *Validation of HF radar data against ADCP measurements*

HF radar data are compared in Fig. 6 with ADCP measurements taken at station FINO-3, which is close to the northern boundary of the radar measurement grid (see Fig. 2). The bottom-mounted ADCP measures

Brought to you by HELMHOLTZ-ZENTRUM GEESTHACHT | Unauthenticated | Downloaded 03/09/21 08:07 AM UTC

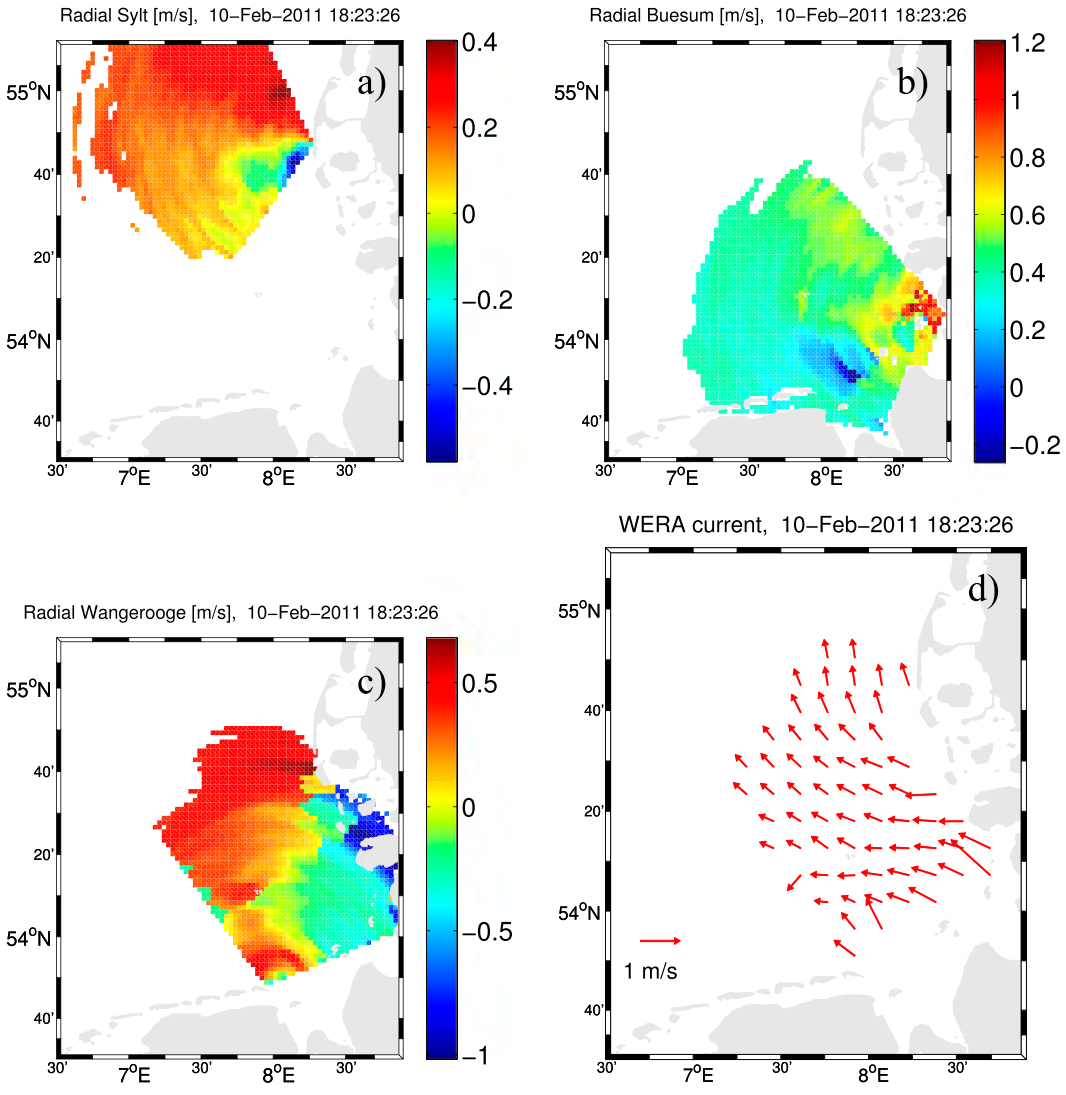

FIG. 5. Example of WERA surface current measurements acquired at 1823 UTC 10 Feb 2011. Shown are the radial components measured by the stations (a) Sylt, (b) Büsum, and (c) Wangerooge, and (d) the derived 2D current vectors.

current speed and direction between 2- and 22-m depths with 2-m intervals. The temporal sampling period is 10 min. The water depth in the area is about 25 m. At the FINO-3 location, only radial current observations from the Sylt station are available. For comparison the radial component was computed from the zonal and meridional component of the ADCP data. Furthermore, it was necessary to use a weighted average of the top three ADCP measurements (2, 4, 6 m) to reduce noise present in the near-surface data. Figure 6 shows comparisons over a period of 13 h on 22 February 2011 (Fig. 6a), as well as a scatter diagram (Fig. 6b) generated from data acquired over 3 months (1 February–1 May 2011). Because of missing values, 2602 collocations of radar and ADCP data were available within this period. With a standard deviation less than 10 cm s^{-1} and a negligible bias, the two datasets are in reasonably good agreement, displaying the dominating tidal periodicity in the area.

3. The numerical circulation model

a. *The model setup*

Numerical simulations were performed using the 3D primitive equation General Estuarine Transport Model (GETM; Burchard and Bolding 2002). This model has been set up in two configurations: a coarse-resolution North Sea–Baltic Sea (3 nmi) model and a one-way nested German Bight model with a horizontal resolution of about 1 km [for the map of nested domains, see Stanev et al. (2011)]. Both models use terrain-following equidistant vertical coordinates (σ coordinates) with 21 nonintersecting layers. The horizontal discretization is

Brought to you by HELMHOLTZ-ZENTRUM GEESTHACHT | Unauthenticated | Downloaded 03/09/21 08:07 AM UTC

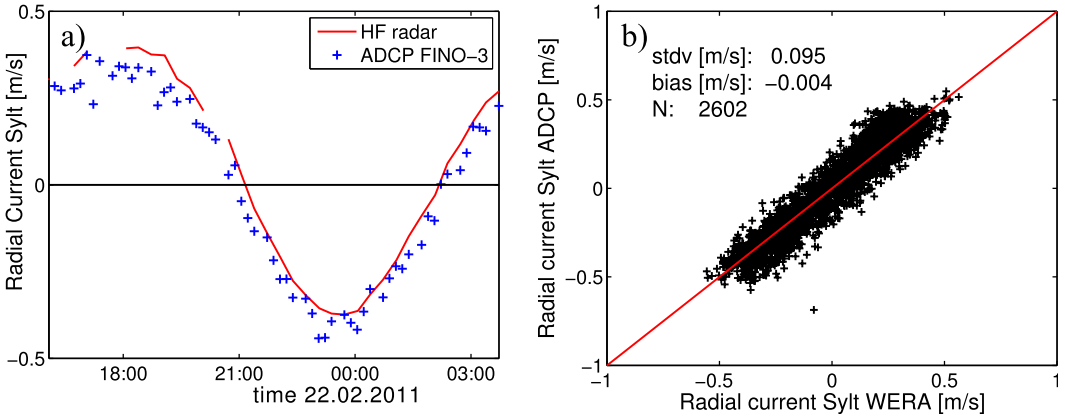

FIG. 6. (a) Comparison of the radial surface current component measured by the Sylt HF radar station (solid line) with the respective ADCP measurements at the FINO-3 platform (crosses) for a period of 13 h. (b) Scatterplot of ADCP- and radar-derived radial components at the Sylt station for the period 1 Feb–1 May 2011.

done on a spherical Arakawa C grid. The bathymetric data for both models are prepared using the ETOPO1 topography and additional observations are made available by the German Hydrographic Service [Bundesamt für Seeschifffahrt und Hydrographie (BSH)].

The model system is forced by 1) the meteorological forcing derived from bulk formulas using wind, mean sea level pressure, air temperature, humidity, and cloud cover taken from the hourly forecasts of the German Weather Service [Deutscher Wetterdienst (DWD)] Consortium for Small Scale Modelling–Europe (COSMO-EU) model with 7-km horizontal resolution; 2) river inflows from climatological data for the 30 most important rivers within the North Sea–Baltic Sea model area, provided by the Swedish Meteorological and Hydrographical Institute (SMHI) and BSH river-runoff data for the German Bight model setup; and 3) time-varying lateral boundary conditions for sea surface elevation, temperature, and salinity. Temperature and salinity of the western and northern open boundaries of the German Bight are taken from the North Sea–Baltic Sea model output; the method proposed by Flather (1976) is used for the barotropic variables. The tidal forcing at the open boundaries of the North Sea–Baltic Sea model toward the Norwegian Sea and the English Channel was constructed using 13 partial tidal constituents obtained from satellite altimeter data via the Oregon State University (OSU) Tidal Inversion software (Egbert and Erofeeva 2002). The model is initialized with data from the operational COSYNA model (www.hzg.de/institutes_platforms/cosyna). The setup is described in more detail by Staneva et al. (2009).

b. German Bight circulation

The circulation of the German Bight has been addressed in numerous studies with a major focus on the numerical modeling of tides (Flather 1976; Maier-Reimer 1977; Backhaus 1980; Davies and Furnes 1980). The works of Staneva et al. (2009) and Port et al. (2011) developed the model presented above, which is used in the data assimilation studies described in the present work. These authors demonstrated that the time-mean circulation in most of the German Bight area is cyclonic, which is mainly due to the dominant eastward wind forcing, that is, a circulation in the direction of propagation of the tidal wave.

In the German Bight, tides are dominated by a Kelvin wave propagating from west to east along the southern boundary and from south to north along the coasts of Germany and Denmark. The amphidromic point is at about 55.5°N, 5.5°E (outside the model area addressed in the present study). The phases at the southwestern and northeastern model boundaries differ by about 120°. The bending of cotidal phase lines seen in Fig. 7a demonstrates the delay of the tidal wave in the coastal region. This delay is largest in front of the Elbe estuary, where a local maximum in the tidal range is also observed. Stanev et al. (2014) revealed the change of spectral composition of tides approaching and entering estuaries and bays of the German Bight. This transformation, as it will be shown later, is also seen in the observations and is due to the nonlinear advection terms, which are responsible for the generation of even harmonic overtides, for instance, M_4, and nonlinear friction, which is responsible for producing odd harmonic overtides, such as M_6. The simulation of the overtide generation is a challenge for the numerical model because of the sensitivity with respect to bottom roughness and small-scale bathymetry features, which are not very well known (Stanev et al. 2014). The resulting errors are larger during spring tides, which are characterized by larger nonlinearities. In the data assimilation part of the present study, an effort will be done to quantify these errors and to correct them in the analysis.

Brought to you by HELMHOLTZ-ZENTRUM GEESTHACHT | Unauthenticated | Downloaded 03/09/21 08:07 AM UTC

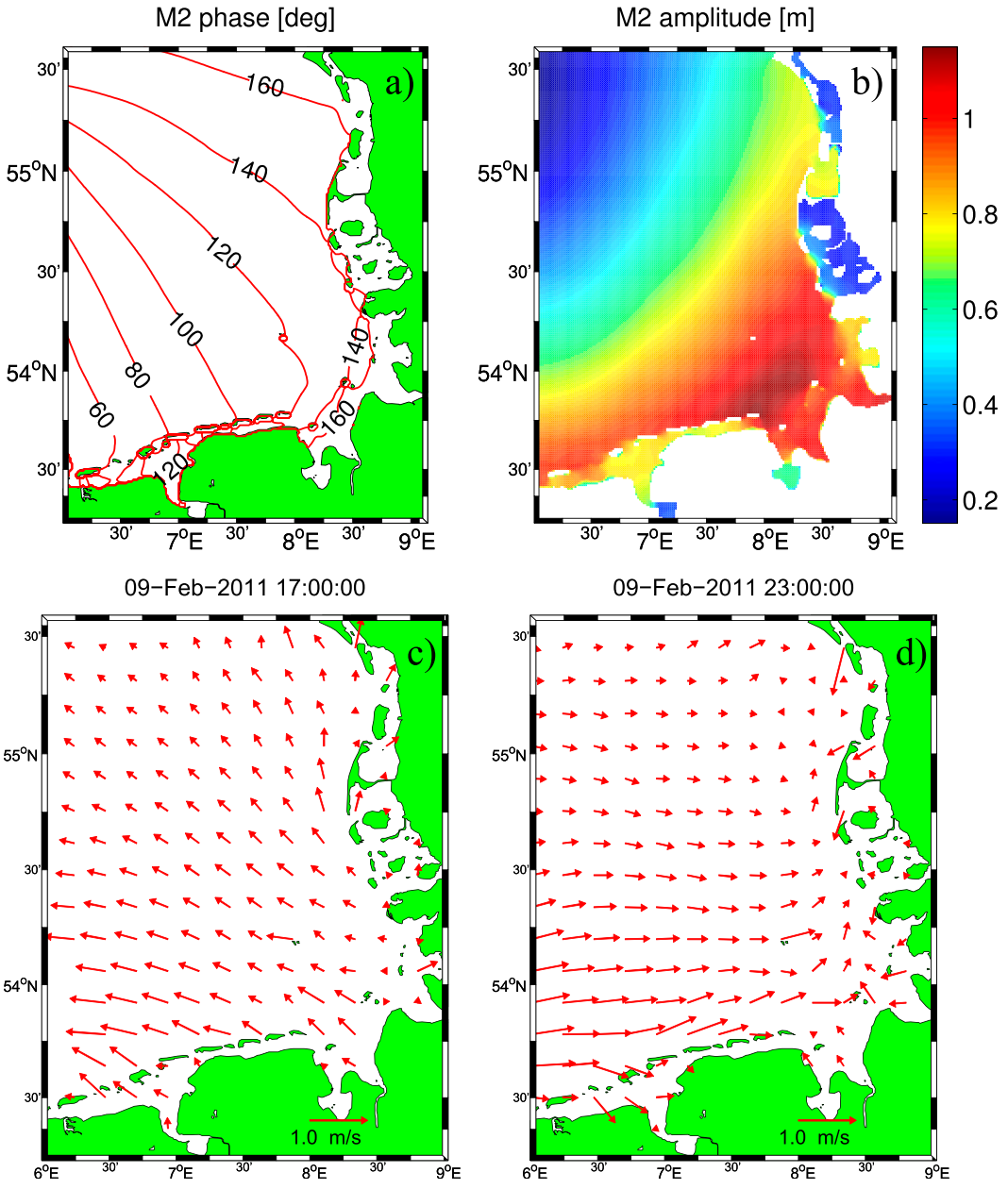

FIG. 7. Cotidal (a) lines and (b) amplitudes for the dominating M_2 tidal constituent estimated from numerical model data for the period 1 Feb–1 May 2011. Surface currents for an (c) outflow and (d) inflow situation at 1700 and 2300 UTC 9 Feb 2011, respectively.

The tidal current can be considered as a back-and-forth motion, which is very pronounced along the southern coast (Figs. 7b–d). Because the incoming tidal wave is partially reflected from the eastern coast, the meridional amplitudes of the tidal wave propagating north farther along the eastern coasts are much lower. Although the general pattern of circulation is relatively simple, the regional variability is quite diverse and challenges the 1) validation against observations covering large areas of the German Bight and 2) deeper insight into the intratidal variability, and state estimates based on a combination of observations and numerical modeling.

4. Blending surface currents from observation and modeling

a. General description

In the following an analysis procedure to blend information from the numerical model and the HF radar data is described. The method uses analysis windows of

Brought to you by HELMHOLTZ-ZENTRUM GEESTHACHT | Unauthenticated | Downloaded 03/09/21 08:07 AM UTC

13-h length for hindcast computations and of 24-h length for short-term forecasts. For forecasts the analysis window is split into a hindcast and a forecast interval. Details about this technique are given in section 4e. The window size is chosen such that at least one tidal cycle is contained in the hindcast interval of the analysis period. Using this approach a continuous surface current trajectory over one or two M_2 tidal cycles is obtained. This is in contrast to the traditional filter approach, where an analysis with a corresponding trajectory jump is performed, whenever observations are available. In a classical filter method, such discontinuities usually occur at the time of the analysis and model restart, because the analysis does not take into account correlations of the model state in time. The proposed blockwise analysis has particular advantages for HF radar data, where measurements are taken at short intervals like 20 min for the radar system used in this study.

To increase the area with available measurements and to avoid any issues related to the processing of two-dimensional current vectors from HF radar data, radial components are used as input for the analysis instead of zonal and meridional components. The main difference from implementations using ensemble Kalman smoother (Barth et al. 2010, 2011) and the technique described in Sakov et al. (2010) is that the model error covariance matrix is estimated from the model background statistics using a longer period of data, and not from an ensemble of model runs. This makes the method easier to implement and less computationally demanding. On the other hand, there are some obvious limitations concerning the type of model errors with which the method can deal.

b. HF radar and model data treatment

In the following, the number of wet grid points (e.g., points that are not permanent land points) in the numerical model will be denoted by q, and the corresponding zonal and meridional surface current components at time step t_k^m denoted by

$$\mathbf{u}(t_k^m) = [u_1(t_k^m), \ldots, u_q(t_k^m)] \quad \text{and} \tag{4}$$

$$\boldsymbol{v}(t_k^m) = [v_1(t_k^m), \ldots, v_q(t_k^m)], \tag{5}$$

respectively, with $k = 1, 2, 3, \ldots$, and the superscript "m" standing for *model*.

These model variables are collected into a single vector $\mathbf{x}$ of dimension $N = 2\,q\,p$ covering an analysis window of p time steps. In parallel we have a vector of radial radar measurements $\mathbf{y}$, acquired by the three stations—Wangerooge, Büsum, and Sylt—within the same period. Both the number of measurements and the observation times in general do not coincide with the model time steps. The only requirement is that the observation time steps are within the analysis interval. Because the radar coverage varies in time, depending on radar transmission and reception conditions, the dimension M of the measurement vector $\mathbf{y}$ usually varies for different analysis periods. A measurement matrix $\mathbf{H}$ of dimension $M \times N$, which relates the state vector $\mathbf{x}$ to the measurements—that is, $\mathbf{y} = \mathbf{Hx}$—is then defined in a straightforward way. If α denotes the angle (anticlockwise vs east) pointing from an antenna station to a certain location, then the radial component u_r at that location is given by

$$u_r = u\cos(\alpha) + v\sin(\alpha), \tag{6}$$

where u and v are the model surface current components. A linear interpolation method is applied to obtain numerical model estimates at the observation times.

c. Observation and model errors

For the application of the Kalman analysis equation, we need estimates for both the observation errors and the model errors. Estimates of observation errors are provided with the standard measurement product as maps of the standard deviation for each time step (for brevity, when we use "error" we mean *rms error*). Following the usual approach, it is assumed that the measurement errors are uncorrelated. One can thus define a diagonal error covariance matrix $\mathbf{R}$ of dimension $M \times M$ containing the error variances for the radial components of all three stations for the entire considered analysis period.

The model errors are not known for the entire model domain (we only have some idea about model errors in the area covered by observation); therefore, we make the assumption that these errors differ from the background statistics only by a constant factor γ (e.g., Bouttier and Courtier 1999), that is,

$$\mathbf{P}_E = \gamma^2 \mathbf{P}_{\mathrm{BG}}, \tag{7}$$

where $\mathbf{P}_E$ and $\mathbf{P}_{\mathrm{BG}}$ are the model error and model background covariance matrices, respectively.

d. EOF decomposition

The dimension of the state vector $\mathbf{x}$ is quite high ($\approx 10^6$); that is, the classical Kalman analysis equation with the full matrix $\mathbf{P}_E$ is not applicable. A reduced rank approximation of the state covariance matrix is therefore estimated by EOF analysis of a period of model simulation, that is,

$$\mathbf{P}_{\mathrm{BG}} = \mathbf{V}\mathbf{U}_f\mathbf{V}^{\mathrm{T}} \tag{8}$$

Brought to you by HELMHOLTZ-ZENTRUM GEESTHACHT | Unauthenticated | Downloaded 03/09/21 08:07 AM UTC

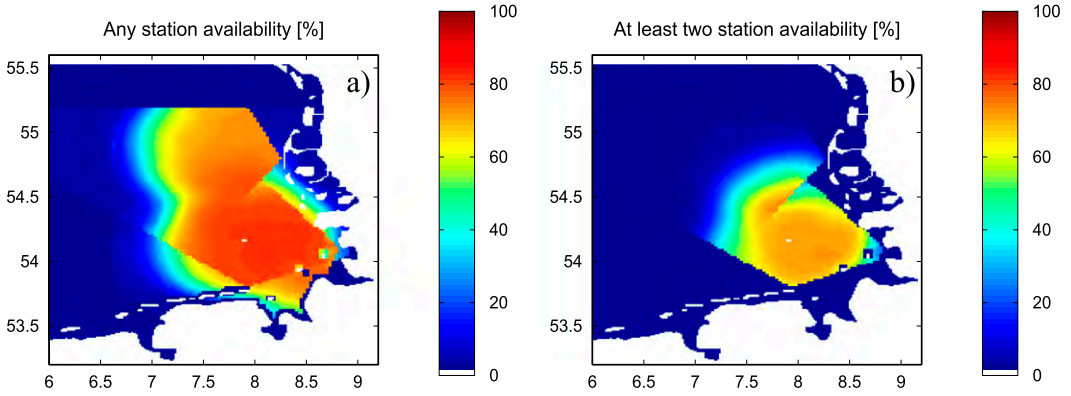

FIG. 8. Data availability from three HF radar stations for Feb/Mar 2011. (a) Availability of at least one radial component. (b) Availability of at least one radial from two HF radar stations. Colors refer to the percentage of available measurements for Feb/Mar 2011. Sharp gradients are due to abrupt change in the number of radars observing neighboring areas.

with an orthogonal matrix $\mathbf{V}$ containing the eigenmodes as columns and a diagonal matrix $\mathbf{U}_f$ with the corresponding eigenvalues, where the subscript "f" stands for *free run*. In this study $\mathbf{P}_{\mathrm{BG}}$ was estimated from a single free model run. By expressing the analysis covariance matrix $\mathbf{P}_a$ in analog form,

$$\mathbf{P}_a = \mathbf{V}\mathbf{U}_a\mathbf{V}^{\mathrm{T}}, \tag{9}$$

we get (Rozier et al. 2007)

$$\mathbf{U}_a^{-1} = \mathbf{U}_f^{-1} + (\mathbf{H}\mathbf{V})^{\mathrm{T}}\mathbf{R}^{-1}H\mathbf{V} \tag{10}$$

with the observation operator H and the observation error covariance matrix $\mathbf{R}$. The Kalman gain matrix is then given as

$$\mathbf{K} = \mathbf{V}\mathbf{U}_a\mathbf{V}^{\mathrm{T}}\mathbf{H}^{\mathrm{T}}\mathbf{R}^{-1} \tag{11}$$

with $\mathbf{V}$ defined by Eq. (8). The subscript a stands for *analysis*. The analyzed state follows as

$$\mathbf{x}_a = \mathbf{x}_f + \mathbf{K}(\mathbf{y} - \mathbf{H}\mathbf{x}_f) \tag{12}$$

with the free-run state vector $\mathbf{x}_f$ and the observation vector $\mathbf{y}$. As the method performs an optimal interpolation (OI) both in time and space, we will refer to the method as the spatiotemporal OI (STOI) method in the following.

e. STOI hindcast

For the analysis in the German Bight, which is dominated by the M_2 tidal signal with a period of 12.4 h, a time window of 13 h (called analysis window in the following) is used. Hourly time steps are used in the model output and in the analysis. To choose the number of time steps p as an odd number has the advantage that one of the analyzed time steps (in this case, time step 7) is exactly in the center of the analysis window. The analysis at this time step is thus influenced by observations in the future and the past in a symmetric way, and will be used as a reference in some of the presented statistics.

This analysis setup results in a state vector with dimension $N = 990\,704$. The dimension M of the measurement vector is of the order of $M \approx 100\,000$ with strong variations depending on radar coverage. To exclude weak, spurious, and unrealistic radar signals from the analysis, two simple quality checks are applied:

1) Only grid points for which at least 50% of the nominal measurements are available (see also Fig. 8) are considered as observation points in the analysis. This criterion is applied to each radar station and for each analysis window separately.
2) Subsequent measurements with unrealistic temporal gradients above $1\,\mathrm{m\,s^{-1}\,h^{-1}}$—that is, $6\,\mathrm{m\,s^{-1}}$ within half of the tidal cycle—are excluded from the analysis.

On average about 15% of the measurements within the analysis period are excluded with a major part due to the first condition.

An EOF decomposition required for the analysis described above [see Eq. (8)] was performed using model output for 3 months (February–April 2011). Seasonal circulation features were not removed prior to the EOF analysis. The analyzed state vector $\mathbf{x}$ is the one introduced above, that is, with dimension $N = 990\,704$. The analysis window was progressed in hourly time steps. The number of analyzed state vectors for the 3-month period was therefore 2160. The dual formalism of Preisendorfer

Brought to you by HELMHOLTZ-ZENTRUM GEESTHACHT | Unauthenticated | Downloaded 03/09/21 08:07 AM UTC

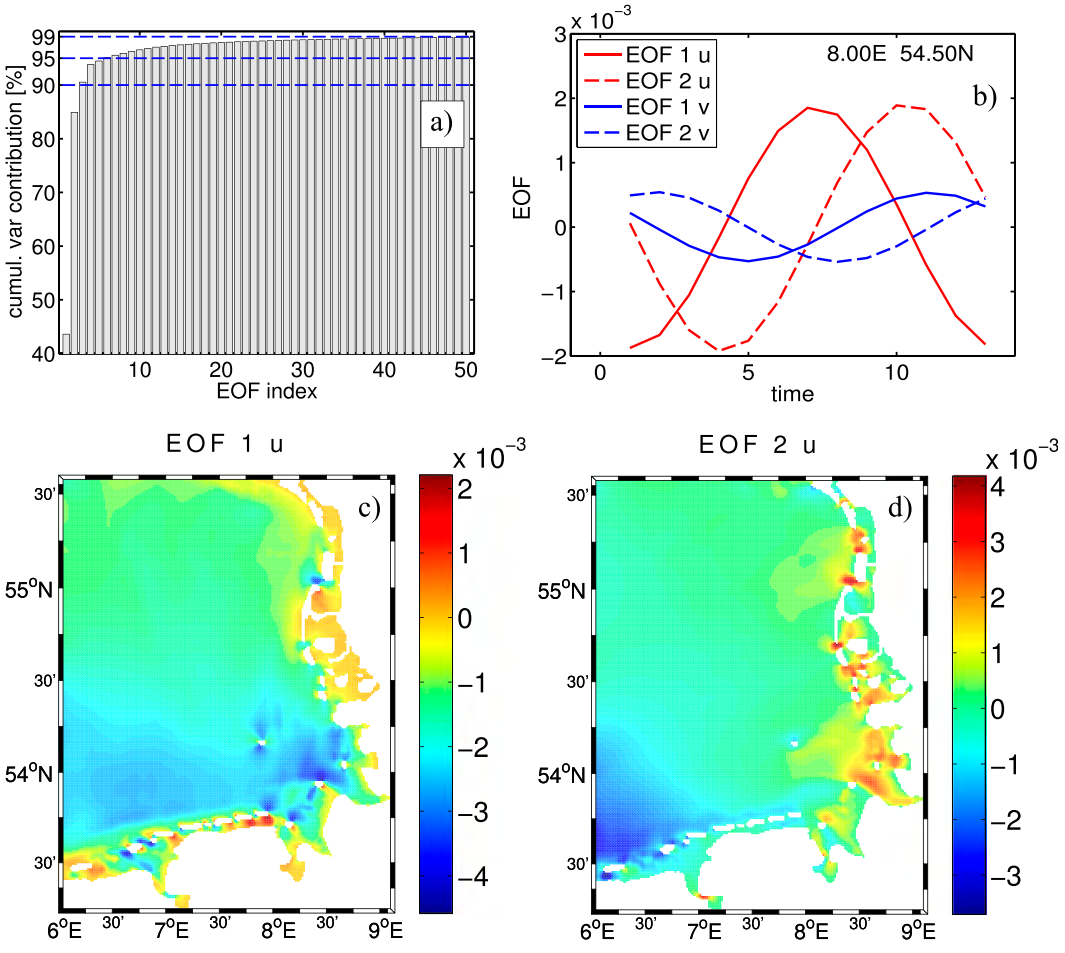

FIG. 9. (a) Cumulative eigenvalue spectrum of the model surface currents obtained for a period of 3 months. (b) First (solid) and second (dashed) EOFs for the zonal (red) and meridional (blue) current components at 54.5°N, 8.0°E. (c) First and (d) second EOFs of the zonal current component. Plots show the first time step of the respective EOFs (see text for details).

(1988) was applied to deal with the large state dimension. The method was run on a Linux machine with eight processors and took about 24 h to complete. It is important to stress that the EOF decomposition has to be done only once in principle. In this study a period of 3 months was used for the EOF analysis, which ensures that a variety of different wind conditions are contained in this time window. The computation of the analysis with precomputed EOFs takes about 1-min computation time and is thus significantly cheaper than a classical model restart technique.

The cumulative EOF spectrum in Fig. 9a demonstrates that the dynamics is dominated by only a few modes; 95% percent of the variance can be explained by the first six EOFs. For the approximation of the covariance matrix $\mathbf{P}_{BG}$, the first 50 EOFs were used, which explained 99% of the variance. The first and second EOFs estimated from the model state at the location 8°E, 54°N, close to the island of Helgoland (Fig. 9b), show about the same variance contribution and with their approximately 3-h time lag, they can be considered as the sine and cosine components, respectively, of the propagating Kelvin wave. The v component has a smaller amplitude than the u component at that location manifesting that a large part of the tidal energy has been lost in the process of transformation of the oscillations from the zonal direction (the incident wave along the southern coast) to the meridional direction (the refracted wave along the eastern coast). The phase shift between the u and v components is one key factor determining the shape of the tidal ellipses discussed in section 6a.

As explained before each of the EOFs contains p time steps. For illustration the first time step of the first and second EOFs is shown in Figs. 9c and 9d, respectively. Both plots refer to the zonal component. Similar to

Brought to you by HELMHOLTZ-ZENTRUM GEESTHACHT | Unauthenticated | Downloaded 03/09/21 08:07 AM UTC

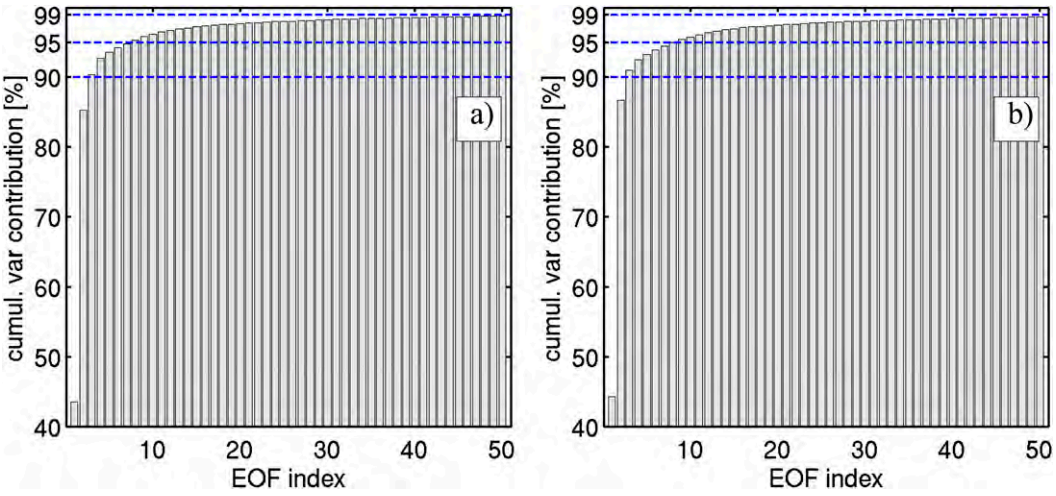

FIG. 10. EOF spectra computed for the periods (a) Jan 1–Mar 31 2011 and (b) 1 Jun–31 Aug 2011.

the time domain, the first and second EOFs basically represent the sine and cosine components, respectively, of the tidal wave passing through the area.

It is obvious that the EOFs are dependent on the period chosen for the estimation. For example, Fig. 10 shows a comparison of EOF spectra computed for the periods 1 January–31 March 2011 (Fig. 10a) and 1 June–31 August 2011 (Fig. 10b). There are some differences visible, but they are below 10% for all components. Experiments using both sets of EOFs in the analysis computations also showed variations below 10% in the corresponding residual errors. The period chosen for the EOF estimation is thus not regarded as a very critical problem at this stage; however, for future fine-tuning and optimization of the methodology, this issue needs to be revisited.

f. STOI forecast

The described analysis method can also be used for the computation of forecasts. Assuming that a forecast from a free run is available, the only difference from the hindcast problem is the missing observations during the forecast period. This method is different from the classical assimilation approach, where a model restart is performed for the forecast horizon using analyzed fields for initialization. The method also differs from classical statistical forecast methods (e.g., Wahle and Stanev 2011), where forecasts are computed based on measurements alone. We will therefore refer to the method as STOI forecast in the following. The method makes sense for forecast problems in which the information provided by the measurements is lost quickly if fed into the model. In a situation where the observation information is dispersed on time scales comparable to the analysis interval, we cannot expect to accumulate information by repeatedly restarting the model with analyzed initial fields. In this case it makes sense to use the original free run as a prior estimate for the forecasts.

A straightforward approach to use the STOI method in an operational setup is to shift the respective time window, including the hindcast and forecast periods, for example, in hourly time steps. In that case a correction of the past and future model states can be carried out based on the model free run (including forecast) and measurements taken during the hindcast period with updates available every hour.

For a short-term forecast, it is reasonable to include additional tidal constituents in the analysis. To achieve this we extended the analysis window to 24 h, which makes sure that tidal components with diurnal periods (K_1, P_1, O_1) are represented in the EOF analysis. To extend the window size even further, special EOF algorithms need to be applied, which were not considered in this study.

Figure 11 demonstrates that the use of an analysis window instead of a stepwise analysis also has advantages in cases of observation data gaps. With stepwise analysis we mean a classical filter approach, where in each analysis step model and observation data from only one single time step are combined. As an example the radial current velocity from HF radar (black crosses), the free model run (blue line), and the STOI analysis (red line) is shown. As one can see, observations are missing for a period of about 4 h. The red circles indicate the analysis one would get from a stepwise analysis method. It is obvious that the STOI method provides an analysis that is in a better consistency with the overall phase shift observed within the period where measurements are available.

Brought to you by HELMHOLTZ-ZENTRUM GEESTHACHT | Unauthenticated | Downloaded 03/09/21 08:07 AM UTC

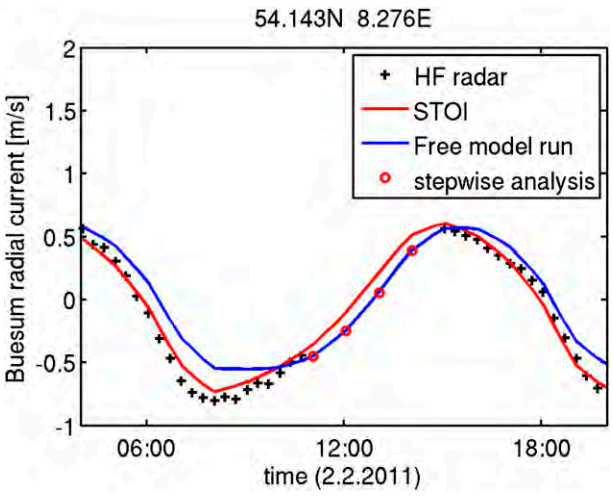

FIG. 11. Radial current velocity from HF radar (black crosses), the free model run (blue line), and the STOI analysis (red line), as well as an analysis obtained with a stepwise approach (red circles). See text for details.

5. Hindcast validation

In this section an example is given for the application of the analysis method described above to data acquired in the German Bight. The analysis makes use of the EOF decomposition. We have used a value of $\gamma = 1/10$ [see Eq. (7)] to specify the model error from the background statistics; that is, we assume that the relative model error is 10%. At the same time we found it necessary to adjust the radar measurement errors given in the observation product (see Fig. 3), which are significantly smaller than the actual errors estimated from comparisons with FINO-3 ADCP data (see the discussion on error estimates). These comparisons are complicated by the additional errors of the ADCP instrument. An exact radar error estimation, which should also include spatial and temporal correlations of the observation errors, is beyond the scope of this paper. With the additional consideration of representation errors (Oke and Sakov 2008), the original observation standard deviations were multiplied by a factor of 5; that is, the matrix **R** was multiplied by a factor of 25. Because of the insufficient knowledge about the true observation and model errors, we can only estimate the order of magnitude. One has to take into account that conceptually the observation error also contains the so-called representation error, which is very difficult to quantify as well (Barth et al. 2010). In summary one can say that the factor of 5 seems to be reasonable as we get the order of magnitude of observation errors indicated by the ADCP comparisons shown in Fig. 6b. It turned out that the spatial and temporal structure of the analysis is not very sensitive to the exact choice of these error estimates. It is obvious that the analysis tends to be closer to the observations if the observation errors are assumed to be small and vice versa. Only if the observation errors are chosen to be very small does the analysis try to reconstruct the current fields over the entire model area from the radar data alone, which is an ill-posed problem, and thus leads to instabilities.

Figure 12 illustrates an analysis performed for the period 0800–2000 UTC 22 March 2011 and a comparison of the surface current fields of the analyzed and original runs for 0800 (Fig. 12a), 1100 (Fig. 12b), 1400 (Fig. 12c), and 1700 UTC (Fig. 12d). Blue arrows refer to the free model run, and red arrows refer to the analysis. The green arrows represent HF radar observations. It is important to remember that the two current components derived from HF radar observations are only available in areas with at least one radial from two stations. Therefore, the area covered by green arrows includes only part of the observed area. For the analysis, radial data from three HF radar stations were used, which provided larger coverage (see Fig. 8). In both the analysis and the free run, we find maximum current magnitudes of close to 1 m s^{-1} with particularly high values in front of the estuaries of the rivers Elbe, Weser, and Ems (see Fig. 1). Differences between the analysis and the free run in terms of magnitude and direction are observed inside, as well as outside the area covered by the radar (cf. Fig. 8). One can see that the analysis leads to an overall improved agreement with the observations.

6. Results and discussion

a. Tidal ellipses parameters

1) USED NOTATIONS

As explained before the proposed method is designed for the treatment of intratidal time scales. For this regime tidal, ellipses are known to provide valuable information on the two-dimensional dynamics of currents. Their geometrical characteristics are indicative of the transformation of tidal signal (Taylor 1922; Hendershott and Speranza 1971). As known from the studies of Carbajal and Pohlmann (2004) and Port et al. (2011), the elliptical properties of the M_2 tide in the German Bight are not only strongly affected by friction but also by the coastal geometry and bottom topography.

Tidal variability can be well described by the standard tidal ellipse parameters. Using complex notation with the imaginary axis pointing in the meridional direction and the real axis pointing in the zonal direction, the temporal evolution of a current vector **v** associated with

Brought to you by HELMHOLTZ-ZENTRUM GEESTHACHT | Unauthenticated | Downloaded 03/09/21 08:07 AM UTC

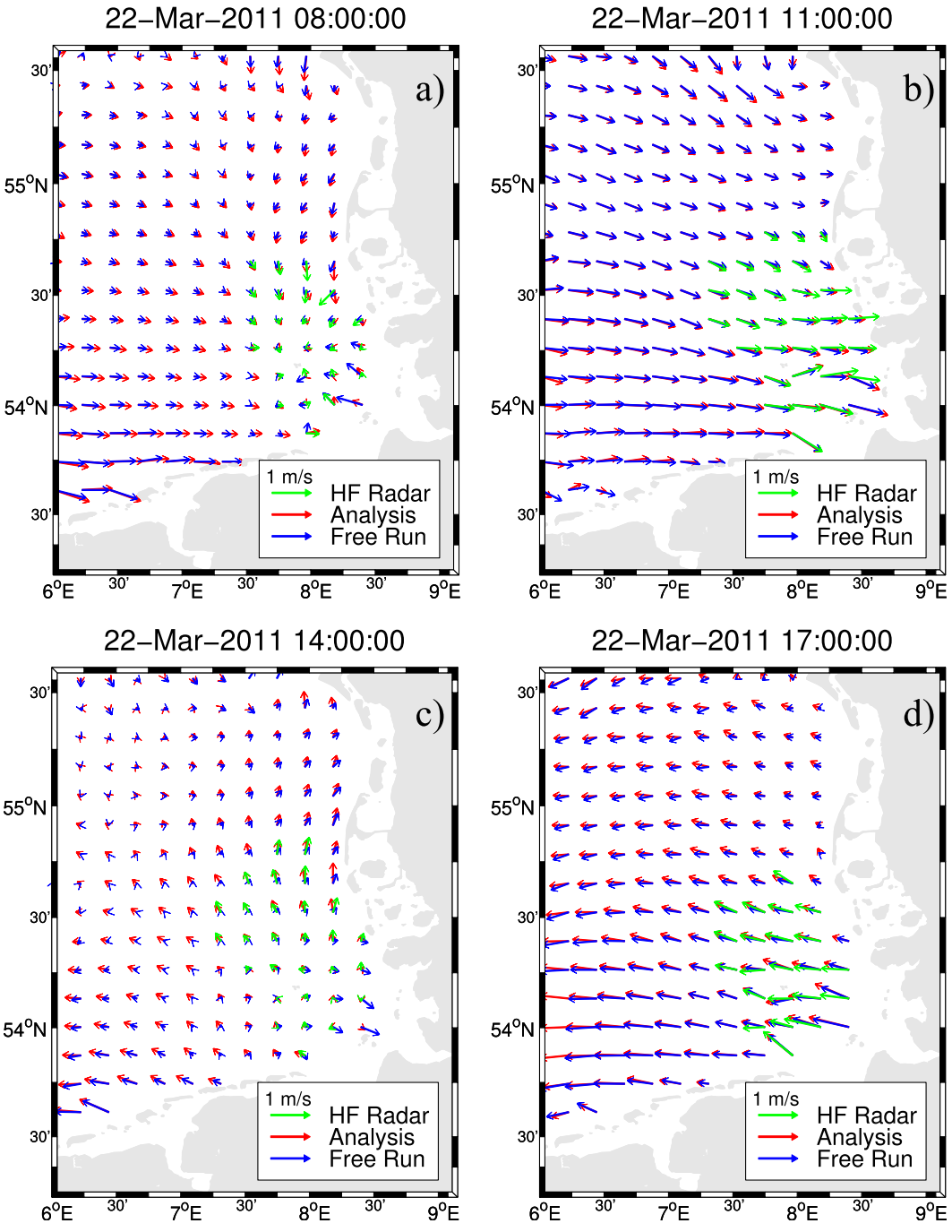

FIG. 12. Illustration of differences between the free run, the analysis, and the HF radar observations for the analysis period 0600–1800 UTC 22 Mar 2011. Times are (a) 0800, (b) 1100, (c) 1400, and (d) 1700 UTC. Red, blue, and green arrows refer to the analysis, free run, and observations, respectively.

the dominating M_2 tidal component can be written as (e.g., Sendner 1952)

$$\mathbf{v}(t) = \{A\cos[\omega_2(t-t_0)] + iB\sin[\omega_2(t-t_0)]\}\exp(i\varphi) \quad (13)$$

with inclination φ, and major and minor axes A and B, respectively. Furthermore, ω_2 denotes the M_2 frequency. The strongest currents with magnitude A occur at time t_0 in the direction φ.

Brought to you by HELMHOLTZ-ZENTRUM GEESTHACHT | Unauthenticated | Downloaded 03/09/21 08:07 AM UTC

In the following we compare the numerical simulations and observations in terms of the standard tidal ellipse parameters.

2) COMPARISON BETWEEN FREE RUN AND ANALYSIS: FOCUS ON NEAP AND SPRING TIDE ERRORS

We will demonstrate in the following 1) the different appearances of tidal ellipses in the German Bight, 2) the differences during spring and neap tides, and 3) the differences between the analysis and the free run.

Tidal ellipsis parameters were estimated for neap and spring tide periods within the time interval 1 February–1 May 2011 for both the free run and the analysis. This was not only done for the dominating M_2 period but also in an analog way for the first harmonic M_4 with a period of 6.21 h. Separate statistics for neap and spring tides were derived by considering only time steps with a time distance of less than 3 days to the nearest neap and spring tides, respectively. The resulting ellipses are shown in Figs. 13a,b for M_2 and in Figs. 13c,d for M_4. The spring tide situation is given on the left and the neap tide situation on the right. For both (spring and neap) periods, the M_2 tidal ellipses in the southern part and the western part of the model area are quite stretched in the west–east direction; that is, the minor axis is relatively small and the inclination is in the east–west direction. The meridional current component is overall smaller than the zonal one, reflecting the basic properties of the Kelvin wave in the studied area (Hendershott and Speranza 1971; Carbajal and Pohlmann 2004; Stanev et al. 2014). The incident wave is characterized by east–west oscillations, which increase in magnitude as the incident wave approaches the East Frisian Islands (along the southern coast, see Fig. 1). After the wave has been redirected along the eastern coast (North Frisian Islands), the zonal oscillations decreased in magnitude and the meridional ones increased but still remaining smaller than the zonal ones. This is also the area where we see larger deviations between the analysis and the free run in terms of inclination and ellipticity. In particular, during spring tide the analysis increases the meridional component in this shallow region. Furthermore, we see a slight clockwise rotation of the inclination in the central part of the region. Stronger differences between neap and spring tides are found for the M_4 component shown at the bottom of Fig. 13. This component is basically generated by nonlinear advection terms, which are increasingly effective with decreasing water depth. This is also reflected in the spatial distribution, where the largest amplitudes can be seen in very shallow water close to the Elbe and Weser estuaries. Again, we can see differences between the analysis and the free run, which are most evident during the spring tide periods.

Obviously, the differences between tidal ellipses (analysis and free run) are indicative of errors in the individual tidal constituents derived from the free run. These errors are largest during the spring tide when the ratio between tidal range and local depth approaches unity. This problem motivates putting further attention on the friction properties in the model and perhaps using better topography and roughness parameterizations. Therefore, the above-mentioned comparison is very useful, because it identifies the areas where the model needs further improvement. One can also interpret the proposed method as a tool to compensate for deficits resulting from imperfect physical parameterizations.

3) COMPARISON WITH OBSERVATIONS

Figure 14 shows a comparison of the M_2 tidal ellipses for the free model run (blue), the analysis (red), and the HF radar (green) estimated for the period 1 February–1 May 2011. The line style refers to the sense of rotation with solid ellipses referring to counterclockwise rotation and dashed ellipses indicating clockwise rotation. For better visualization only the area where HF radar data are available is shown. One can see that the analysis is closer to the observations, in particular in the northern part, which is characterized by relatively smooth bathymetry. In the Elbe and Weser estuaries, the flow is strongly steered by the bathymetry and the analysis stays very close to the free run. In addition one can see that the sense of rotation is anticlockwise in both the analysis and the HF radar in most of the region except the Elbe and Weser estuaries. This effect has already been observed in Carbajal and Pohlmann (2004) and seems to be caused by the shape of the coastline (embayments) in combination with the complex bathymetry (Stanev et al. 2014).

b. STOI performance in hindcast mode: Residuals and innovation

In this section a statistical analysis is performed for the innovations and residuals. Results using an analysis window of 13-h length are presented. Analysis windows of 24-h length will then be used in the subsequent section for the computation of forecasts.

The innovation

$$\mathrm{IN}(t) = y_{\mathrm{obs}}(t) - \mathbf{H}x_{\mathrm{free}}(t) \tag{14}$$

measures the mismatch between the free run and the observations. The analysis residual

$$\mathrm{AR}(t) = y_{\mathrm{obs}}(t) - \mathbf{H}x_{\mathrm{analysis}}(t) \tag{15}$$

Brought to you by HELMHOLTZ-ZENTRUM GEESTHACHT | Unauthenticated | Downloaded 03/09/21 08:07 AM UTC

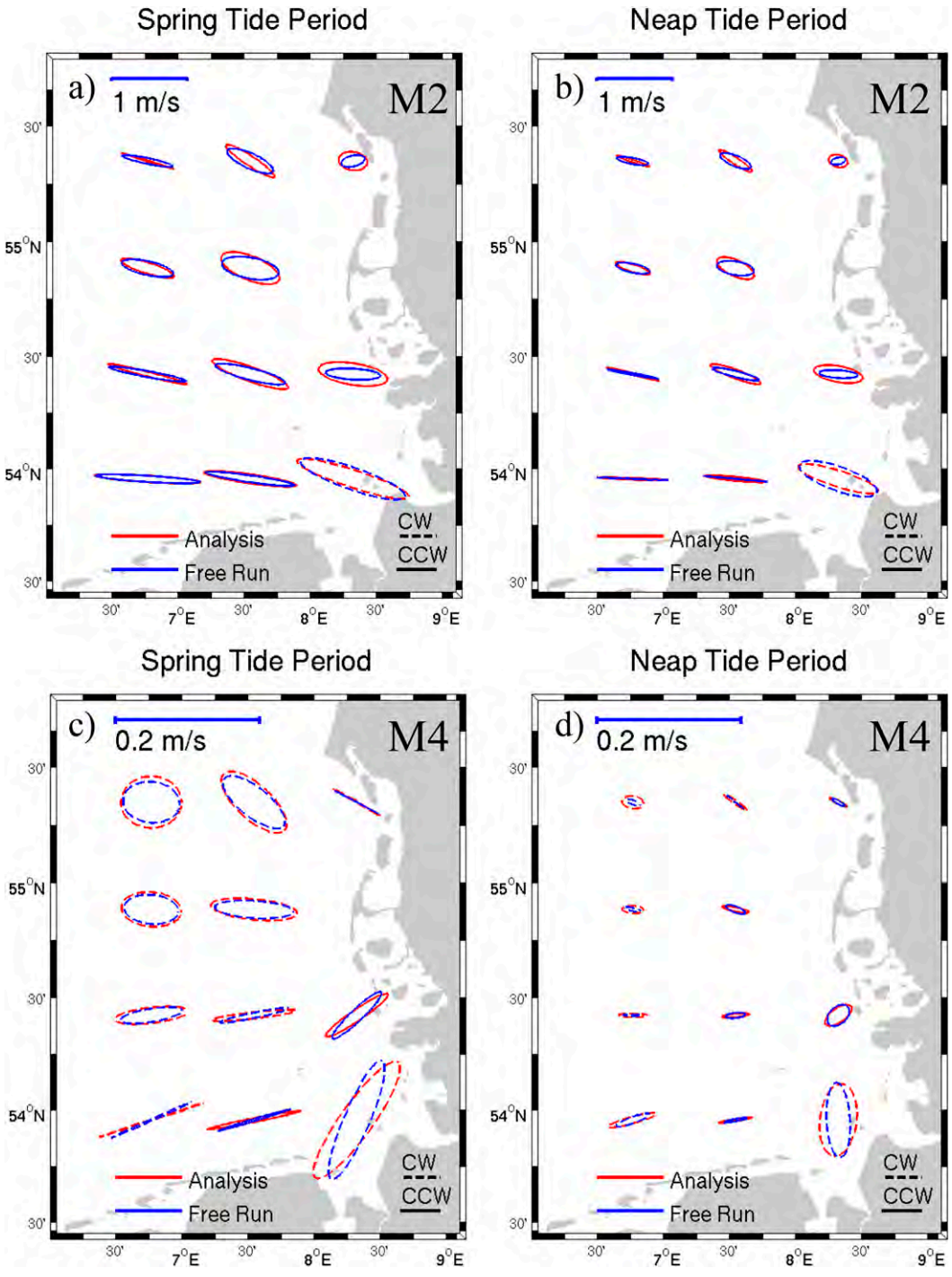

FIG. 13. Comparison of (a),(b) M_2 and (c),(d) M_4 tidal ellipses computed from the free run (blue) and the analysis (red) for (left) spring tides and (right) neap tides within the period 1 Feb–1 May 2011 (see text for details).

measures the mismatch between the analysis and the observations. According to the definition of the observation operator H (see section 4d), both quantities are based on differences between observed and simulated radials rather than the u and v components. The comparison of IN and AR shows to what extend the analysis is able to bring the simulations from the free run closer to the observations and how far the analysis is from the observations. The deviations between the free model run, the analysis, and the observations

Brought to you by HELMHOLTZ-ZENTRUM GEESTHACHT | Unauthenticated | Downloaded 03/09/21 08:07 AM UTC

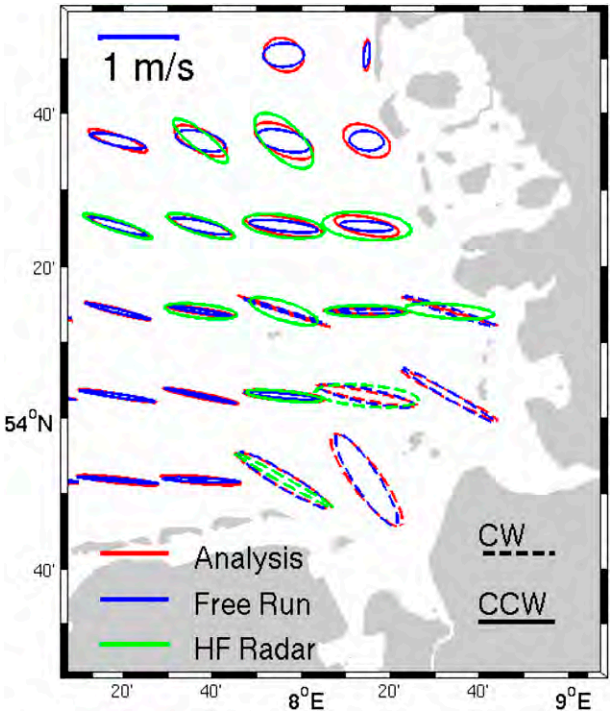

FIG. 14. Comparison of M_2 tidal ellipses for the free model run (blue), the analysis (red), and the HF radar (green) estimated for the period 1 Feb–1 May 2011. Dashed and solid ellipses refer to clockwise and counterclockwise sense of rotation, respectively.

were computed in the root-mean-square error sense; that is,

$$\overline{\mathrm{AR}} = \sqrt{\langle \mathrm{AR}^2 \rangle_t} \quad \text{and} \tag{16}$$

$$\overline{\mathrm{IN}} = \sqrt{\langle \mathrm{IN}^2 \rangle_t}, \tag{17}$$

where $\langle \cdot \rangle_t$ denotes the temporal mean. The comparisons were carried out for time step 7 within the 13-h analysis period; that is, the analyzed fields are centered within the analysis window. The basic reasoning for the choice of 13 h is that this is the minimum size required to reasonably correct the phase and amplitude of the dominant M_2 tidal component. On the other hand, it turned out that for hindcasts, longer analysis windows do not seem to lead to further improvements of practical value. The use of longer analysis windows, however, is useful for the computations of forecasts, as we will see in the next section. A summary of the spatially averaged innovations and residuals is given in Table 1.

The maps showing innovations and residuals for the radial components of all three antenna stations (Fig. 15) reveal a considerable reduction of errors in the analysis and justify using STOI when developing products for

TABLE 1. Spatially and temporally averaged innovations (IN; $\mathrm{m\,s^{-1}}$) and analysis residuals (AR; $\mathrm{m\,s^{-1}}$), and percentage reduction (Red.) in the radial component differences after analysis with respect to the three radar stations for spring and neap tide periods.

	$\mathrm{IN}^{\mathrm{SPRING}}$	$\mathrm{AR}^{\mathrm{SPRING}}$	Red.	$\mathrm{IN}^{\mathrm{NEAP}}$	$\mathrm{AR}^{\mathrm{NEAP}}$	Red.
Sylt	0.10	0.071	31	0.095	0.065	32
Büsum	0.185	0.147	21	0.167	0.130	22
Wangerooge	0.173	0.131	25	0.162	0.121	25

surface currents from observations and modeling. In the example shown, the relative error reductions vary between 20% and 40%, with the strongest reduction found for the Sylt station. This is most likely due to the fact that the Sylt radar covers an area with a relatively smooth bathymetry. The complex bathymetry in the southeastern part of the model area and around the island of Helgoland leads to higher errors already in the free run for the Büsum and Wangerooge stations. The higher complexity of the background statistics in this area makes error reductions in the analysis more demanding.

The horizontal rms patterns of the innovations and residuals demonstrate that the analysis leads to a significant reduction of the misfit between the numerical model and observations from all three radar stations. In the majority of the grid points, the magnitude of the residual is less than half of the one of the innovation (see Table 1 for the area mean estimates). In some other areas, an improvement is not achieved. This is evident in the very shallow water areas of the Elbe and Weser estuaries and at the eastern boundary of the area covered by the Wangerooge antenna. As explained above, the complex bathymetry in the Wadden Sea (that is, the region between the North and East Frisian Islands and the coast; see Fig. 1) provides one source of errors; another source is due to the insufficient model resolution near the coast (1 km used in the model), which makes it difficult to adequately simulate all important processes in this coastal zone. This would justify using higher-resolution models in the future.

c. *STOI performance in forecasting mode*

A comparison between the free run and the analysis with radar observations were carried out for the forecast mode, as well. Spatial averages were computed for the area where both current components are available from the HF radar (see Fig. 8b). As explained before, it makes sense to use a longer analysis window in this case to capture more tidal constituents. We have chosen a 24-h window length as a compromise between computational costs and analysis performance. Figure 16 shows a comparison of the analysis behavior for forecast periods of

Brought to you by HELMHOLTZ-ZENTRUM GEESTHACHT | Unauthenticated | Downloaded 03/09/21 08:07 AM UTC

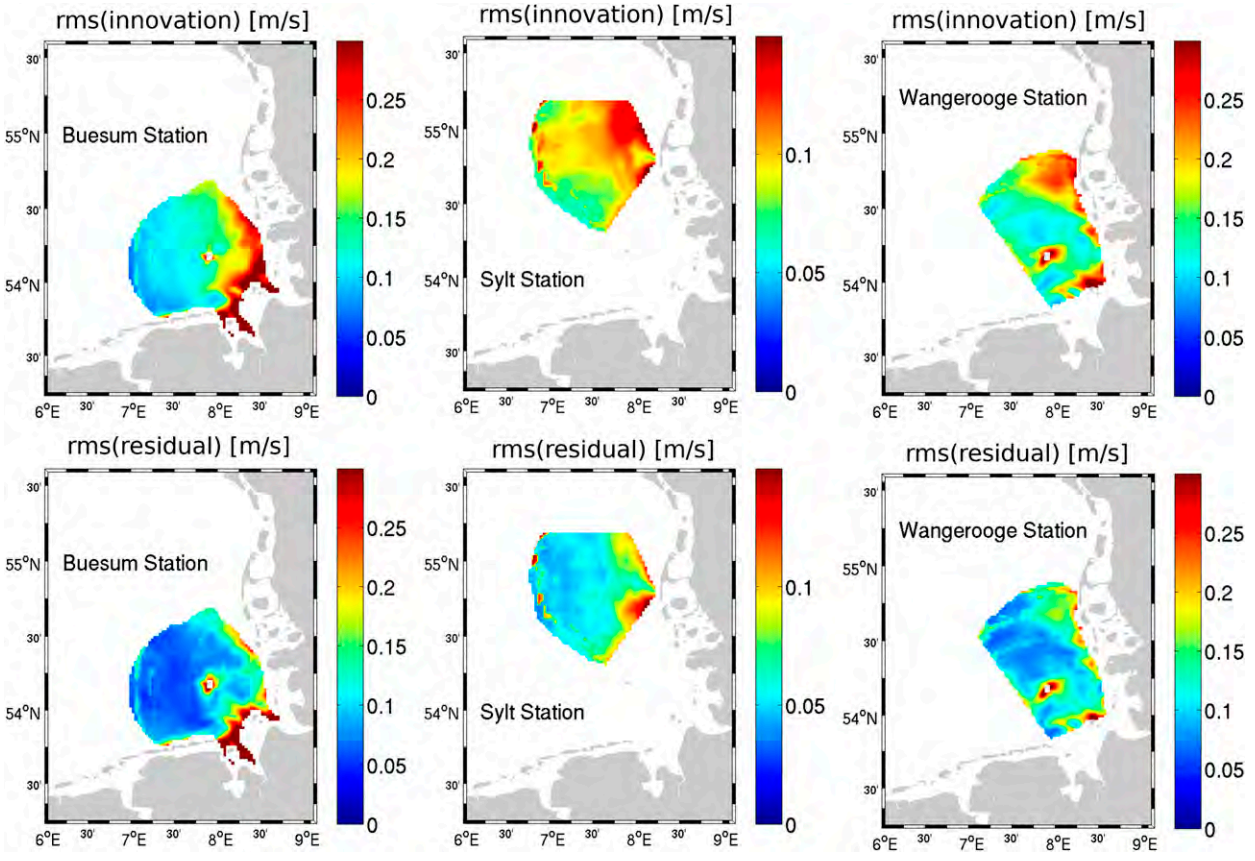

FIG. 15. RMS difference between the free run (top row) and the analysis (bottom row) in terms of the radial components for the Büsum station (left), the Sylt station (center), and the Wangerooge station (right). The statistics refer to the period 1 Feb–1 May 2011.

6 h (Figs. 16a,b) and 12 h (Figs.16c,d). Skills for the zonal (left) and the meridional (right) current components were computed as

$$\text{skill}_u = 1 - \frac{\langle (u_a - u_{\text{hf}})^2 \rangle}{\langle (u_f - u_{\text{hf}})^2 \rangle} \quad \text{and} \tag{18}$$

$$\text{skill}_v = 1 - \frac{\langle (v_a - v_{\text{hf}})^2 \rangle}{\langle (v_f - v_{\text{hf}})^2 \rangle}, \tag{19}$$

respectively, where (u_a, v_a) is the analyzed current field, $(u_{\text{hf}}, v_{\text{hf}})$ is the observed current field, and (u_f, v_f) is the free-run current field. Both skills are shown (red curves) together with the skill of the persistence (blue curves), that is, keeping the current field constant after the forecast time $t = 0$. The skills represent averages for the period 1 February–1 May 2011. For better visualization the persistence skill was divided by a factor of 40 and 10 for the u and v components, respectively.

As one can see, the analysis is able to improve the forecast over both the 6- and 12-h forecast horizons for both current components. In particular, the analysis performs better than persistence, which has negative skills for the entire forecast period. More details about how to interpret skills in tidal environments are given in the appendix.

The relatively large negative skill values for the u component persistence can be explained by the smaller relative innovation errors of the u component. The absolute innovation errors (spatial averages) of the u and v components are comparable with rms values between 0.15 and 0.2 m s^{-1}. However the amplitude of the u component is significantly larger than of the v component (see Fig. 14). For the persistence this means that the denominators in Eqs. (18) and (19) are similar, but the nominator in the u equation is larger than the one in the v component, leading to larger negative skill values. This effect is further amplified by the use of squared errors in the skill definition. Because of the dominant M_2 tidal period of 12.42 h, the state at some time $t = 0$ is a relatively good estimate for the state 12 h later. This is reflected in the shape of the persistence curve for the 12-h forecast, which is discussed in more detail in the appendix.

It is also evident that the forecast performance of the analysis is quite variable within the forecast interval.

Brought to you by HELMHOLTZ-ZENTRUM GEESTHACHT | Unauthenticated | Downloaded 03/09/21 08:07 AM UTC

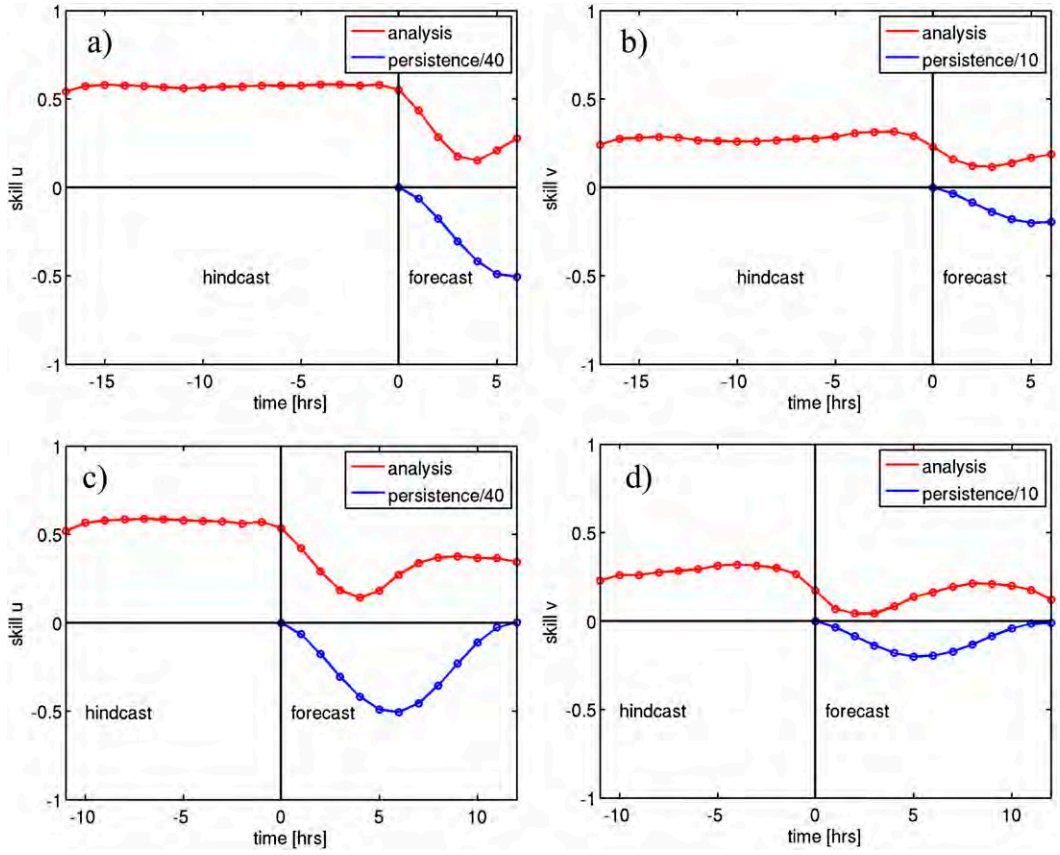

FIG. 16. Skills of the analysis (red) and the persistence (blue) for (top) 6- and (bottom) 12-h forecasts. Separate skills are given for the (left) zonal and (right) meridional current components. For better visualization the skills for the persistence are divided by 40 and 10 for the u and v components, respectively.

This is not a surprise considering the highly variable dynamics of the system, which goes through a complete ebb–flood cycle within the 12-h forecast period. As seen in Fig. 16, the analysis skill curves have a minimum at around 90° of the M_2 tidal cycle; that is, they are phase shifted with respect to the persistence skill curves by about 3 h. To explain this we will assume that there is slack water at the analysis time $t = 0$. Then, about 3 h later, we would observe high current speeds, that is, a completely different situation. A correction of these strong currents using data with the last available observations coming from a situation with very small current speeds 3 h before is, of course, a challenge. This is a likely explanation for the drop of skill around about the 3-h forecast time. In summary one can say that the skill curves represent a complicated mixture of the periodic effect just mentioned and the continuous skill degradation that is to be expected with increasing forecast times.

Concerning the difference between the skill for the u and v components, it is important to emphasize that the dynamics in the German Bight are strongly anisotropic [see, e.g., Fig. 14; sections 3b and 6a(2)] with a much stronger zonal current than a meridional current. There are indications (e.g., Stanev et al. 2014) that the meridional component is very sensitive to small bathymetry uncertainties, in particular west of the North Frisian Islands–Wadden Sea. It can then also be expected that the achieved improvements and hence the skill for the meridional component are smaller than for the zonal component, reflecting the dependence of the used methods on the EOFs derived from the free model run.

The spatial distributions of the 6-h hindcast skill and the 12-h forecast skill are shown in Fig. 17. In this case the skill refers to the total two-dimensional vector, that is,

$$\text{skill} = 1 - \frac{\langle (u_a - u_{\text{hf}})^2 + (v_a - v_{\text{hf}})^2 \rangle}{\langle (u_f - u_{\text{hf}})^2 + (v_f - v_{\text{hf}})^2 \rangle}. \qquad (20)$$

As expected the hindcast skill is overall higher than the forecast skill. One can also see that the skill is positive almost everywhere except in a region around the island of Helgoland. This region is known for its complex bathymetry and dynamics, and there is a possibility that the

Brought to you by HELMHOLTZ-ZENTRUM GEESTHACHT | Unauthenticated | Downloaded 03/09/21 08:07 AM UTC

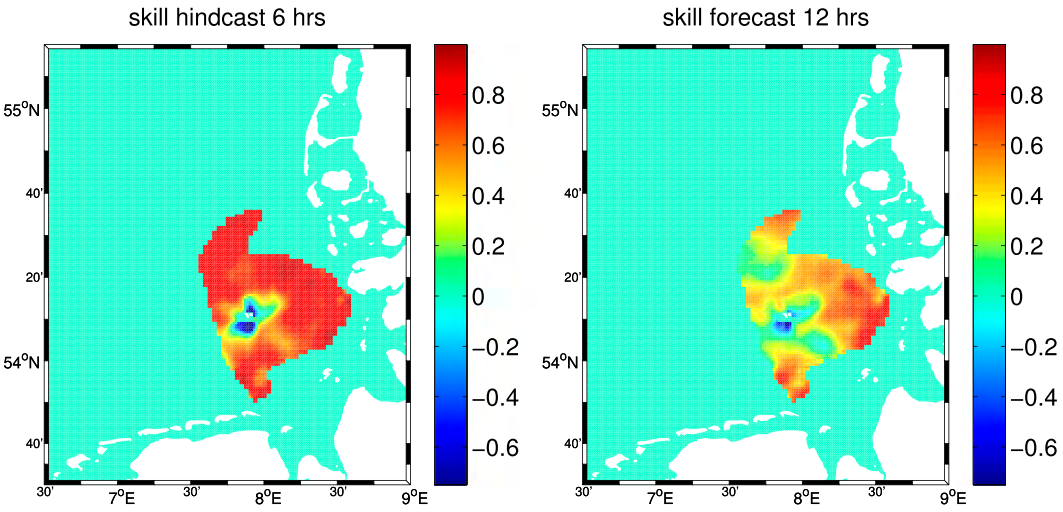

FIG. 17. Skill map of (left) 6-h hindcast and (right) 12-h forecast. Skill values refer to total current vectors (see text for details).

background statistics given by the free model run are not realistic enough in that area.

d. Validation against ADCP observations

In the following the free run and the analysis are compared to ADCP in situ data acquired at the FINO-3 platform (Fig. 18) for the period 1600 UTC 22 February–0400 23 February. Both the zonal (left) and the meridional (right) current component are improved by the analysis. The corresponding statistical parameters (standard deviation and root-mean-square error) derived for the period 1 February–1 May 2011 are summarized in Table 2 for both current components. The rms error contains both the bias and the standard deviation errors.

Again, the statistical parameters are given for analyzed current fields, which were derived for time step 7 within the analysis window; that is, the analysis window is centered around the fields considered in the statistics. Obviously, the analysis leads to an improvement of the state estimates in terms of standard deviation and rms in all cases. To put these improvements into perspective, it is important to stress that only the radial current component provided by the Sylt station is available at the FINO-3 station; that is, information from the background statistics about correlations of the u and v components is required for the analysis.

e. Upscaling capabilities

Another aspect revealing the benefit of using STOI is demonstrated below on the example of its skill to improve state estimates out of the area covered by HF radars. One such location where ADCP observations are available is the FINO-1 platform, which is in the western part of the model area (see Fig. 2). The water

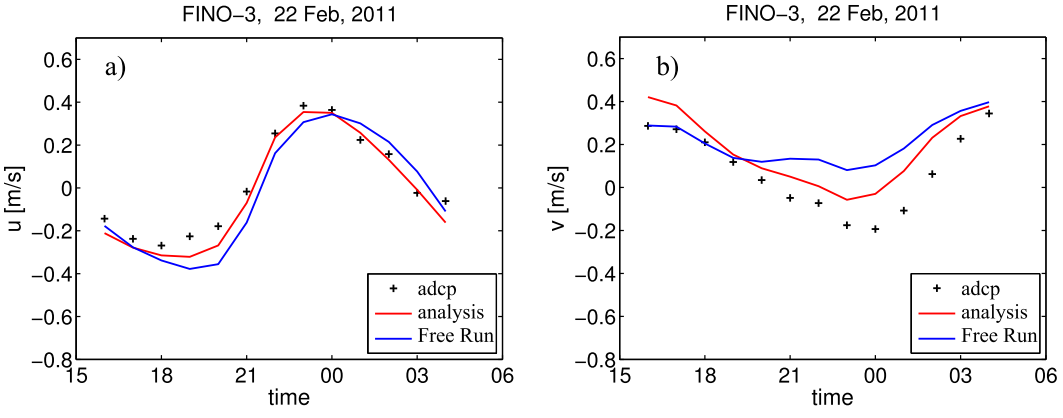

FIG. 18. Comparison of the analysis (red) and the free run (blue) with ADCP measurements (black crosses) taken at the FINO-3 platform for the (left) zonal and (right) meridional surface current components.

Brought to you by HELMHOLTZ-ZENTRUM GEESTHACHT | Unauthenticated | Downloaded 03/09/21 08:07 AM UTC

TABLE 2. Comparison of free run and analysis with respect to FINO-3 ADCP measurements ($m\,s^{-1}$; using a weighted average of the top three near-surface measurements). Averages were estimated for the period 1 Feb–1 May 2011.

sim-FINO3	Free run	Analysis
stdv u	0.122	0.097
stdv v	0.125	0.101
rms u	0.122	0.097
rms v	0.126	0.103

depth at that location is about 30 m, and current measurements are available with a vertical spacing of 2 m. Because no measurements were available from this platform for the period discussed above, the analysis presented in the following is for 1 September–1 December 2011. It is noteworthy that the results presented below are essentially different from the ones in Fig. 18, in the sense that no HF radar data exist in this location.

The comparison of the free model run and the analysis to ADCP data (Fig. 19) demonstrates that the analysis is in fact able to correct a phase and amplitude error of the free model run in this case. Table 3 shows a comparison of the free run and the analysis with ADCP surface current measurements in terms of the rms differences. As one can see the analysis leads to an improved agreement with the observations both for the zonal and meridional current component also in statistical terms. To put these relatively small improvements into perspective, it is important to remember that the ADCP data are affected by observation errors. In fact Fig. 6b gives a good idea about the challenge of achieving a consistent picture using ADCP and HF radar data.

The above-mentioned result is proof that the proposed method has upscaling capabilities, in the sense that the information in the coastal area is propagated outside the observed area. These capabilities are basically due to the temporal and spatial properties of dominant processes, which are well captured by the used EOFs. This fundamental result opens the issue about the "communication" between the open ocean prediction systems and the coastal ones. The need for further studies in this field stems from the fact that 1) many of the coastal prediction systems use one-way nested models—that is, the ocean prediction systems are not impacted by the coastal ones; and 2) specific coastal observations like data from HF radar are not effectively used in ocean predictions—that is, their use in ocean predictions could be beneficial.

f. Overall assessment of STOI

The analysis is able to improve the free run for the hindcast period and for most of the forecast period, as demonstrated in Fig. 20, showing the skill for the hindcast and forecast. The statistics is given for the hindcast period (hours 1–18) in Fig. 20a and for the forecast period (hours 19–24) in Fig. 20b. Again, the skill refers to the total two-dimensional vector in this case [see Eq. (20)] and was estimated by averaging over the area where both currents' components were available from the radar. One can see that the analysis leads to improvements both for the hindcast and the forecast most of the time. For some short periods, we have zero skill due to missing observation data; that is, the analysis is identical to the free run in that case.

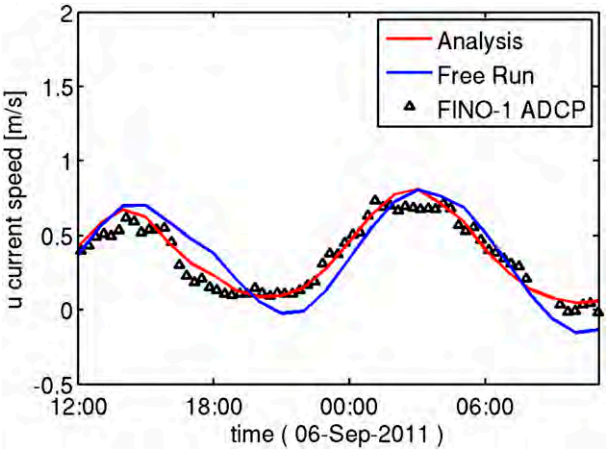

FIG. 19. Comparison of the analysis (red) and the free run (blue) with ADCP measurements (black triangles) taken at the FINO-1 platform for the zonal surface current component.

The errors are quite variable with correlation times comparable to correlation scales found in the atmospheric wind forcing. It is therefore very likely that the observed variability in the rms values reflects different error characteristics of the numerical model depending on wind conditions. This issue (see also Kim et al. 2009), different contexts of which have been addressed for the area of German Bight by Barth et al. (2011) and Port et al. (2011), however, is beyond the scope of this paper and will be addressed in a separate study.

7. Conclusions

Important results from this study are 1) method development tailored to a specific observational platform and applied in coastal operational oceanography, and

TABLE 3. Comparison of free run and analysis with FINO-1 ADCP measurements ($m\,s^{-1}$) acquired between 1 Sep and 1 Dec 2011.

(sim-FINO1)	Free run	Analysis
rms u	0.2371	0.2268
rms v	0.2638	0.2591

Brought to you by HELMHOLTZ-ZENTRUM GEESTHACHT | Unauthenticated | Downloaded 03/09/21 08:07 AM UTC

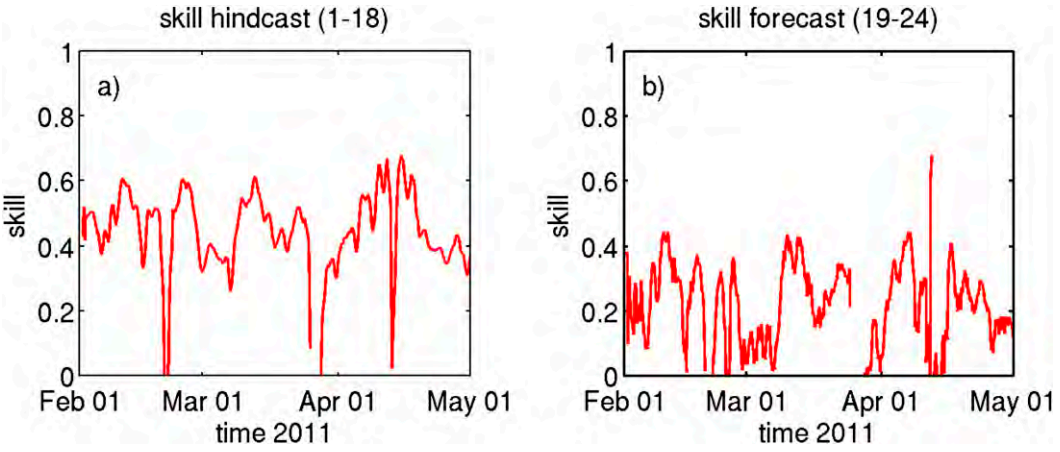

FIG. 20. Area mean skills for (a) the hindcast period (hours 1– 18) and (b) the forecast period (hours 19–24) for the period 1 Feb–1 May 2011. Skill values refer to the total 2D current vector (see text for details).

2) improved understanding of German Bight dynamics and deficiencies of numerical models for this area.

With respect to the first overall result, new developments using ongoing data acquisitions by an operational network of three WERA stations with relatively large area coverage and high resolution in time and space were described. Details about the HF radar instrument and data processing, and intercomparisons between different measurements were presented. The major focus of this study was on the intratidal scales. This was justified by the specificity of most ocean coasts, which are exposed to tides, and by the practical needs to provide short-term coastal ocean nowcasts and forecasts with specified errors.

The heart of the present study was the new method proposed to blend numerical models and HF radar observations in an efficient and dynamically consistent way. It aimed at avoiding the problems encountered when applying standard model restart techniques for barotropic variables in tide-dominated areas. Thus, it enabled a relatively straightforward solution to address data assimilation at intratidal time scales. The formalism used spatiotemporal optimal interpolation (STOI) and benefited largely from smoother techniques employed so far in various coastal and ocean applications. At the same time it was computationally efficient, robust, and easy to implement. The key difference between the STOI method and other techniques, which provide surface current fields based on HF radar data alone (e.g., Kim et al. 2007, 2008), was that the estimates described in this study were dynamically consistent with a numerical model run. This was achieved using an EOF approach, which makes sure that the temporal and spatial correlation patterns of the applied state corrections are in accordance with the model dynamics reflected in the background error covariance matrix.

The STOI validation showed good skill not only in the area covered by HF radar observations but also outside it, revealing its upscaling capabilities. The use of HF radar data in the STOI system made it possible to generate homogeneous and continuous 2D current fields over the entire model area that were of superior quality in comparison to a free model run. This was considered an important aspect when using such methods in operational systems, of which many have numerical models as their core part.

STOI can also be used for improved predictions in the coastal ocean. When applied for short-term forecasting, it used first-guess information from a numerical model forecast and could therefore be regarded as an extension of methods, where predictions are made based on HF radar observations alone (e.g., Wahle and Stanev 2011).

Results for the period February–March 2011, which were presented in this study as an example illustrating the performance of STOI, demonstrated that HF radar data assimilation could enhance the coastal ocean prediction capabilities by making use of observations and modeling. Such improvements could prepare the ground for developing new data products in the coastal ocean. Finally, the operational use of HF radar data could support research and development in setting up optimal and cost-efficient environmental monitoring programs. One theoretical study on this issue has been presented by Schulz-Stellenfleth and Stanev (2010).

With respect to the second overall result of the present study, it is noteworthy that the previous works in the area of the German Bight used either pointwise observations or numerical modeling, or interpretation of HF radar observations with nonoptimal positioning of antennas, less data coverage, and relatively short duration of operation. It was demonstrated that a combination of HF radar data and

Brought to you by HELMHOLTZ-ZENTRUM GEESTHACHT | Unauthenticated | Downloaded 03/09/21 08:07 AM UTC

numerical model results can provide a deeper insight into the German Bight dynamics. In particular, homogeneous maps of surface currents based on observations and numerical modeling well captured the dominant processes of nonlinear distortion of the Kelvin waves.

The results presented about tidal ellipses and temporal–spatial characteristics of the tidal wave demonstrated a relatively good consistency between model and observations. In both the model data and the HF radar observations, tidal ellipses appeared quite stretched in the west–east direction. Their sense of rotation was anticlockwise in most of the model area, both in the analysis and the HF radar observations. The reversal of the rotation (from anticlockwise to clockwise) shown by the observed and simulated tidal ellipses near the Elbe estuary proved that the balances between the dominant forces were well captured by the model.

The meridional current was overall smaller than the zonal one; the latter was due to the fact that the incident wave, which is the major forcing in the considered area, was characterized by east–west oscillations. The refraction of the wave along the eastern coast resulted in a decrease of the zonal oscillations and an increase of the meridional ones. The largest differences between the neap and spring tide oscillations were found for the M_4 component in the coastal zone. This was an indication that both observations and simulations captured the relative increase of the nonlinear advection terms over the shallows.

The comparisons between analysis and free run demonstrated also that the generation of overtides in the model left space for improvements in many cases. The errors were larger during spring tides, which resulted from the larger nonlinearities during this period. This gave a useful indication of where further model developments (improvements) are needed. One such improvement is expected after giving further consideration to the friction properties in the model and perhaps using better topography and roughness parameterizations. This expectation is supported by the fact that the analysis was closer to the observations in the northern part of the model area, which was characterized by relatively smooth bathymetry.

In summary, one can say that the proposed method is in fact able to improve short-term forecasts of surface currents with significantly less computational effort than standard assimilation approaches. It has therefore big potential for practical applications like search and rescue operations and contaminant drift forecasts. The technique can be extended in different directions. For example, one of the problems, which was not addressed here, was the optimization of open boundary conditions (Barth et al. 2010) and atmospheric forcing (Barth et al. 2011; Kim et al. 2009). As explained before, there is also a need to further improve the error estimates for both numerical models and observations. Another subject of future research is the impact of the surface current analysis on temperature and salinity.

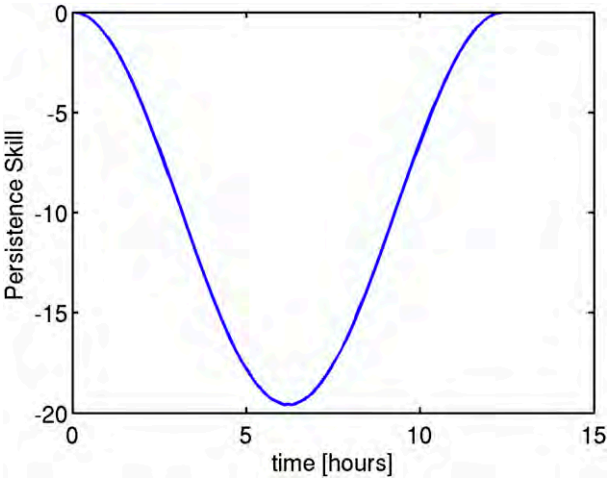

FIG. A1. Theoretical persistence skill.

Acknowledgments. This work has been carried out in the frame of COSYNA and profited largely from the MyOcean-2 and JERICO project. Data were made available by BSH and DWD. Thanks are due to A. Barth for the stimulating discussions.

APPENDIX

Interpretation of Forecast Skills in Tidal Environments

The main shape of the persistence skill curve in Fig. 16 and the fact that it is negative most of the time can be explained by the periodicity of the currents. Let us approximate the ''true'' current velocity by a cosine function, that is,

$$u(t) = A\cos(\omega t + \varphi), \tag{A1}$$

where ω is the M_2 period and φ is some phase angle. The free model run is then given by

$$u^f(t) = A\cos(\omega t + \varphi) + \eta(t) \tag{A2}$$

with some model error η. Likewise, the observations are given by

$$u^{\text{obs}} = A\cos(\omega t + \varphi) + \epsilon \tag{A3}$$

with some observation error ϵ. For the numerator in the skill definition [Eqs. (18) and (19)], we then get

Brought to you by HELMHOLTZ-ZENTRUM GEESTHACHT | Unauthenticated | Downloaded 03/09/21 08:07 AM UTC

$$\begin{aligned}\langle (u^{\text{pers}} - u^{\text{obs}})^2 \rangle &= \langle [A\cos(\varphi) - A\cos(\omega t + \varphi) + \eta(t) - \epsilon]^2 \rangle \\ &= \frac{A^2}{2\pi}\int_0^{2\pi} [\cos(\varphi) - \cos(\omega t + \varphi)]^2 \, d\varphi + \langle \eta^2(0) \rangle + \langle \epsilon^2 \rangle \\ &= A^2[1 - \cos(\omega t)] + \langle \eta^2(0) \rangle + \langle \epsilon^2 \rangle, \end{aligned} \tag{A4}$$

where we assume that the model and observation errors are independent. Using some typical values $\langle \eta^2(0) \rangle \approx \langle \eta^2(t) \rangle \approx 0.1^2\,\text{m}^2\,\text{s}^{-2}$, $\langle \epsilon^2 \rangle \approx 0.05^2\,\text{m}^2\,\text{s}^{-2}$, and $A = 0.35\,\text{m}\,\text{s}^{-1}$, we get the skill curve shown in Fig. A1, which is quite close to the curve actually estimated in the realistic case (Fig. 16).

REFERENCES

Backhaus, J., 1980: Simulation von Bewegungsvorgängen in der Deutschen Bucht. *Dtsch. Hydrogr. Z.,* **15,** 7–56.

Barrick, D. E., 1978: HF radio oceanography—A review. *Bound.-Layer Meteor.,* **13,** 23–43, doi:10.1007/BF00913860.

——, 2008: 30 years of CMTC and CODAR. *IEEE/OES 9th Working Conference on Current Measurement Technology,* IEEE, 131–136.

Barth, A., A. Alvera-Azcárate, and R. Weisberg, 2008: Assimilation of high-frequency radar currents in a nested model of the West Florida Shelf. *J. Geophys. Res.,* **113,** C08033, doi:10.1029/2007JC004585.

——, ——, K.-W. Gurgel, J. Staneva, A. Port, J.-M. Beckers, and E. Stanev, 2010: Ensemble perturbation smoother for optimizing tidal boundary conditions by assimilation of high-frequency radar surface currents—Application to the German Bight. *Ocean Sci.,* **6,** 161–178, doi:10.5194/os-6-161-2010.

——, ——, J.-M. Beckers, J. Staneva, E. V. Stanev, and J. Schulz-Stellenfleth, 2011: Correcting surface winds by assimilating high-frequency radar surface currents in the German Bight. *Ocean Dyn.,* **61,** 599–610, doi:10.1007/s10236-010-0369-0.

Bennet, A. F., 2002: *Inverse Modelling of the Ocean and Atmosphere.* Cambridge University Press, 260 pp.

Bouttier, F., and P. Courtier, 1999: Data assimilation concepts and methods. Meteorological Training Course Lecture Series, ECMWF, 59 pp.

Breivik, O., and O. Sætra, 2001: Real time assimilation of HF radar currents into a coastal ocean model. *J. Mar. Syst.,* **28,** 161–182, doi:10.1016/S0924-7963(01)00002-1.

Burchard, H., and K. Bolding, 2002: GETM: A general estuarine transport model. European Commission Joint Research Centre Tech. Rep. EUR 20253 EN, 157 pp.

Carbajal, N., and T. Pohlmann, 2004: Comparison between measured and calculated tidal ellipses in the German Bight. *Ocean Dyn.,* **54,** 520–530, doi:10.1007/s10236-004-0096-5.

Davies, A., and G. Furnes, 1980: Observed and computed M_2 tidal currents in the North Sea. *J. Phys. Oceanogr.,* **10,** 237–257, doi:10.1175/1520-0485(1980)010<0237:OACMTC>2.0.CO;2.

Egbert, G., and S. Erofeeva, 2002: Efficient inverse modeling of barotropic ocean tides. *J. Atmos. Oceanic Technol.,* **19,** 183–204, doi:10.1175/1520-0426(2002)019<0183:EIMOBO>2.0.CO;2.

Evensen, G., 2007: *Data Assimilation: The Ensemble Kalman Filter.* Springer, 279 pp.

Flather, R., 1976: A tidal model of the north-west European continental shelf. *Mem. Soc. Roy. Sci. Lige Ser. 6,* **10,** 141–164.

Frolov, S., J. Paduan, M. Cook, and J. Bellingham, 2012: Improved statistical prediction of surface currents based on historic HF-radar observations. *Ocean Dyn.,* **62,** 1111–1122, doi:10.1007/s10236-012-0553-5.

Frost, J. R., and L. D. Stone, 2001: Review of search theory: Advances and applications to search and rescue decision support. U.S. Coast Guard Research and Development Center Rep. CG-D-15-01, 127 pp.

Gandin, L., 1965: *Objective Analysis of Meteorological Fields.* Israel Program for Scientific Translations, 242 pp.

Glenn, S., and O. Schofield, 2009: Growing a distributed ocean observatory: Our view from the cool room. *Oceanography,* **22,** 128–145, doi:10.5670/oceanog.2009.44.

Gopalakrishnan, G., and A. F. Blumberg, 2012: Assimilation of HF radar-derived surface currents on tidal-timescales. *J. Oper. Oceanogr.,* **5,** 75–87.

Gurgel, K.-W., 1994: Shipborne measurement of surface current fields by HF radar. *L'Onde Electr.,* **74,** 54–59.

——, and T. Schlick, 2008: Land-based over-the-horizon radar techniques for monitoring the north-east Atlantic coastal zone. *Remote Sensing of the European Seas,* V. Barale, Ed., Springer, 447–460.

——, and ——, 2009: Remarks on signal processing in HF radars using FMCW modulation. *Proceedings: International Radar Symposium; IRS 2009,* H. Rohling, Ed., Deutsche Gesellschaft für Ortung und Navigation, 63–67.

——, G. Antonischki, H.-H. Essen, and T. Schlick, 1999a: Wellen Radar (WERA): A new ground-wave based HF radar for ocean remote sensing. *Coastal Eng.,* **37,** 219–234, doi:10.1016/S0378-3839(99)00027-7.

——, H.-H. Essen, and S. P. Kingsley, 1999b: HF radars: Physical limitations and recent developments. *Coastal Eng.,* **37,** 201–218, doi:10.1016/S0378-3839(99)00026-5.

Hackett, B., A. Breivik, and C. Wettre, 2006: Forecasting the drift of objects and substances in the oceans. *Ocean Weather Forecasting: An Integrated View of Oceanography,* E. P. Chassignet and J. Verron, Eds., Springer, 507–524.

Harlan, J., E. Terrill, L. Hazard, C. Keen, D. Barrick, C. Whelan, S. Howden, and J. Kohut, 2010: The Integrated Ocean Observing System high-frequency radar network: Status and local, regional, and national applications. *Mar. Technol. Soc. J.,* **44,** 122–132, doi:10.4031/MTSJ.44.6.6.

Hendershott, M. C., and A. Speranza, 1971: Co-oscillating tide in long, narrow bays: The Taylor problem revisited. *Deep-Sea Res. Oceanogr. Abstr.,* **18,** 959–980, doi:10.1016/0011-7471(71)90002-7.

Hunt, B., and Coauthors, 2004: Four-dimensional ensemble Kalman filtering. *Tellus,* **56A,** 273–277, doi:10.1111/j.1600-0870.2004.00066.x.

Ivanov, L., and O. Melnichenko, 2005: Determination of mesoscale surface currents in shallow-water regions according to the data of high-frequency radar measurements. *Phys. Oceanogr.,* **15,** 92–104, doi:10.1007/s11110-005-0033-2.

Kim, S. Y., E. J. Terrill, and B. D. Cornuelle, 2007: Objectively mapping HF radar-derived surface current data using measured and idealized data covariance matrices. *J. Geophys. Res.,* **112,** C06021, doi:10.1029/2006JC003756.

Brought to you by HELMHOLTZ-ZENTRUM GEESTHACHT | Unauthenticated | Downloaded 03/09/21 08:07 AM UTC

——, ——, and ——, 2008: Mapping surface currents from HF radar radial velocity measurements using optimal interpolation. *J. Geophys. Res.,* **113,** C10023, doi:10.1029/2007JC004244.

——, B. D. Cornulelle, and E. J. Terril, 2009: Anisotropic response of surface currents to the wind in a coastal region. *J. Phys. Oceanogr.,* **39,** 1512–1533, doi:10.1175/2009JPO4013.1.

Kurapov, A., G. Egbert, J. Allen, R. Miller, S. Erofeeva, and P. Kosro, 2003: The M_2 internal tide off Oregon: Inferences from data assimilation. *J. Phys. Oceanogr.,* **33,** 1733–1757, doi:10.1175/2397.1.

Lewis, J., I. Shulman, and A. Blumberg, 1998: Assimilation of Doppler radar current data into numerical ocean models. *Cont. Shelf Res.,* **18,** 541–559, doi:10.1016/S0278-4343(98)00006-5.

Li, Z., Y. Chao, J. McWilliams, and K. Ide, 2008: A three-dimensional variational data assimilation scheme for the Regional Ocean Modeling System. *J. Atmos. Oceanic Technol.,* **25,** 2074–2090, doi:10.1175/2008JTECHO594.1.

Maier-Reimer, E., 1977: Residual circulation in the North Sea due to the M_2-tide and mean annual wind stress. *Dtsch. Hydrogr. Z.,* **30,** 69–80, doi:10.1007/BF02227045.

Moore, A. M., H. G. Arango, G. Broquet, B. S. Powell, A. T. Weaver, and J. Zavala-Garay, 2011: The Regional Ocean Modeling System (ROMS) 4-dimensional variational data assimilation systems: Part I—System overview and formulation. *Prog. Oceanogr.,* **91,** 34–49, doi:10.1016/j.pocean.2011.05.004.

Oke, P., and P. Sakov, 2008: Representation error of oceanic observations for data assimilation. *J. Atmos. Oceanic Technol.,* **25,** 1004–1017, doi:10.1175/2007JTECHO558.1.

——, J. Allen, R. Miller, G. Egbert, and P. Kosro, 2002: Assimilation of surface velocity data into a primitive equation coastal ocean model. *J. Geophys. Res.,* **107,** 3122, doi:10.1029/2000JC000511.

Paduan, J. D., and L. K. Rosenfeld, 1996: Remotely sensed surface currents in Monterey Bay from shore-based HF radar (Coastal Ocean Dynamics Application Radar). *J. Geophys. Res.,* **101,** 20 669–20 686, doi:10.1029/96JC01663.

——, and I. Shulman, 2004: HF radar data assimilation in the Monterey Bay area. *J. Geophys. Res.,* **109,** C07S09, doi:10.1029/2003JC001949.

Port, A., K.-W. Gurgel, J. Staneva, J. Schulz-Stellenfleth, and E. Stanev, 2011: Tidal and wind-driven surface currents in the German Bight: HFR observations versus model simulations. *Ocean Dyn.,* **61,** 1567–1585, doi:10.1007/s10236-011-0412-9.

Preisendorfer, R., 1988: *Principal Component Analyses in Meteorology and Oceanography.* Developments in Atmospheric Sciences, Vol. 17, Elsevier, 444 pp.

Proctor, R., and M. Howarth, 2008: Coastal observatories and operational oceanography: A European perspective. *Mar. Technol. Soc. J.,* **42,** 10–13, doi:10.4031/002533208786842534.

Rozier, D., F. Birol, E. Cosme, P. Brasseur, J. Brankart, and J. Verron, 2007: A reduced-order Kalman filter for data assimilation in physical oceanography. *SIAM Rev.,* **49,** 449–465, doi:10.1137/050635717.

Sakov, P., G. Evensen, and L. Bertino, 2010: Asynchronous data assimilation with the EnKF. *Tellus,* **62A,** 24–29, doi:10.1111/j.1600-0870.2009.00417.x.

Schulz-Stellenfleth, J., and E. V. Stanev, 2010: Statistical assessment of ocean observing networks: A study of water level measurements in the German Bight. *Ocean Modell.,* **33,** 270–282, doi:10.1016/j.ocemod.2010.03.001.

Scott, R., J. Allen, G. Egbert, and R. Miller, 2000: Assimilation of surface current measurements in a coastal ocean model. *J. Phys. Oceanogr.,* **30,** 2359–2378, doi:10.1175/1520-0485(2000)030<2359:AOSCMI>2.0.CO;2.

Sendner, H., 1952: Ein Verfahren zur Berechnung von Gezeitenstrom- und Gefällsellipsen. *Dtsch. Hydrogr. Z.,* **5,** 199–205, doi:10.1007/BF02020305.

Sentchev, A., M. Yaremchuk, and F. Lyard, 2006: Residual circulation in the English Channel as a dynamically consistent synthesis of shore-based observations of sea level and currents. *Cont. Shelf Res.,* **26,** 1884–1904, doi:10.1016/j.csr.2006.06.006.

Stanev, E., J. Schulz-Stellenfleth, J. Staneva, S. Grayek, J. Seemann, and W. Petersen, 2011: Coastal observing and forecasting system for the German Bight—Estimates of hydrophysical states. *Ocean Sci.,* **7,** 569–583, doi:10.5194/os-7-569-2011.

——, R. Al-Nadhairi, J. Staneva, J. Schulz-Stellenfleth, and A. Valle-Levinson, 2014: Tidal wave transformations in the German Bight. *Ocean Dyn.,* **64,** 951–968, doi:10.1007/s10236-014-0733-6.

Staneva, J., E. V. Stanev, J.-O. Wolff, T. H. Badewien, R. Reuter, B. Flemming, A. Bartholomä, and K. Bolding, 2009: Hydrodynamics and sediment dynamics in the German Bight. A focus on observations and numerical modeling in the East Frisian Wadden Sea. *Cont. Shelf Res.,* **29,** 302–319, doi:10.1016/j.csr.2008.01.006.

Stewart, R. H., and J. W. Joy, 1974: HF radio measurements of surface currents. *Deep-Sea Res. Oceanogr. Abstr.,* **21,** 1039–1049, doi:10.1016/0011-7471(74)90066-7.

Taylor, G. I., 1922: Tidal oscillations in gulfs and rectangular basins. *Proc. London Math. Soc.,* **S2-20,** 148–181, doi:10.1112/plms/s2-20.1.148.

Teague, S. S., Z. R. Vesecky, and Z. R. Hallock, 2001: A comparison of multifrequency HF radar and ADCP measurements of near-surface currents during COPE-3. *IEEE J. Oceanic Eng.,* **26,** 399–404, doi:10.1109/48.946513.

van Leeuwen, P., 2001: An ensemble smoother with error estimates. *Mon. Wea. Rev.,* **129,** 709–728, doi:10.1175/1520-0493(2001)129<0709:AESWEE>2.0.CO;2.

Wahle, K., and E. Stanev, 2011: Consistency and complementarity of different coastal ocean observations: A neural network-based analysis for the German Bight. *Geophys. Res. Lett.,* **38,** L10603, doi:10.1029/2011GL047070.

Wilkin, J., H. G. Arango, D. B. Haidvogel, C. S. Lichtenwalner, S. M. Glenn, and K. S. Hedström, 2005: A regional ocean modeling system for the Long-term Ecosystem Observatory. *J. Geophys. Res.,* **110,** C06S91, doi:10.1029/2003JC002218.

Willis, Z., 2012: Towards a global HF radar network. *J. Oper. Oceanography,* **5,** 2.

Yaremchuk, M., and A. Sentchev, 2009: Mapping radar-derived sea surface currents with a variational method. *Cont. Shelf Res.,* **29,** 1711–1722, doi:10.1016/j.csr.2009.05.016.

Zhang, W., J. Wilkin, and H. Arango, 2010a: Towards an integrated observation and modeling system in the New York Bight using variational methods. Part I: 4DVAR data assimilation. *Ocean Modell.,* **35,** 119–133, doi:10.1016/j.ocemod.2010.08.003.

——, ——, and J. Levin, 2010b: Towards an integrated observation and modeling system in the New York Bight using variational methods. Part II: Representer-based observing strategy evaluation. *Ocean Modell.,* **35,** 10–13, doi:10.1016/j.ocemod.2010.06.006.

Brought to you by HELMHOLTZ-ZENTRUM GEESTHACHT | Unauthenticated | Downloaded 03/09/21 08:07 AM UTC